The International Journal of

ENERGY & ENGINEERING SCIENCES

GAZIANTEP UNIVERSITY

May, 2017
Issue: 2
Volume: 2

Energy Systems Engineering Publications
Gaziantep University, TURKEY

Editor In Chief Asst. Prof. Dr. Adem Atmaca
Co-Editor Asst. Prof. Dr. Nihat Atmaca

Gaziantep University Engineering Faculty
+90 342 360 12 00
+90 342 360 10 13
gaziantep.university.ijees@gmail.com
https://uemk-conferences.wixsite.com/ijees

Published by

Gaziantep university, Engineering Faculty, Energy Systems Engineering, Üniversite Bulvarı 27310 Şehitkamil - Gaziantep, TÜRKİYE

ISSN

Table of Contents

COMPARISON OF AISC 360 – 16 AND EC4 FOR THE PREDICTION OF COMPOSITE COLUMN CAPACITY

Baraa J.M. AL-Eliwi, Ph.D. student
Civil Engineering Department, University of Gaziantep, 27310 Gaziantep, Turkey
Civil Engineering Department, University of Mosul, 41001 Mosul, Iraq
baraa.aleliwi@gmail.com

Talha Ekmekyapar, Ph.D
Civil Engineering Department, University of Gaziantep, 27310 Gaziantep, Turkey
ekmekyapar@gantep.edu.tr

Hussein A.M.S. Al-Juboori, M.Sc student
Civil Engineering Department, University of Gaziantep, 27310 Gaziantep, Turkey
hussainjuboori@gmail.com

ABSTRACT: Composite constructions are used widely in civil engineering structures. The steel and concrete act together to resist the loads. Composite columns are a significant application of composite construction, and the Concrete-Filled Steel Tube (CFST) columns are the most common type of composite columns. The CFST columns have been increasingly used all over the world due to their inherent advantages, and in particular because of their favorable behavior under seismic loads. The steel tube effectively confines the concrete core, providing a highly ductile response under compression and a high energy absorption capacity. This type of composite column has been used primarily in bridges, reservoirs, and tall buildings. Circular CFST column provides much more effective confinement to the core concrete than other types of column sections under axial load due to an enhancement of composite action between steel tube and core concrete. Many design specifications used to predict the capacity of CFST columns, the ANSI/AISC 360 – 16 and the Eurocode 4 (EC4). The ANSI/AISC 360 – 16 is the specification for steel structures in the United States; the Eurocode 4 is the European code for composite structure design, respectively. The objective of this study is to investigate the differences between the AISC 360-16 and the EC4 approaches of circular CFST columns under axial load and to evaluate how well they model the actual column behavior through a series of statistical comparisons. Also, the parameters which are used in design specification calculations steps will be assessed. The important parameters in calculations will also be specified to underline the best way in the design field.

Key words: Composite columns, CFST column, Axial capacity, ANSI/AISC 360 – 16, EC4.

INTRODUCTION

Composite structures term is widely used in civil engineering structures where the steel and concrete formed together into an element. The aim is to achieve the best level of performance than would have been case had the two materials functioned separately.
Composite columns are very important part of composite structures; the term "composite column" refers to any compression member which a steel element acts compositely with the concrete element so that both elements resist compressive forces. There is a wide variety of column types of various cross – section, but the most commonly used are the concrete-encased composite columns, and the concrete filled steel tube columns, Figure 1 (Giakoumelis and Lam, 2004; Liang, 2014).

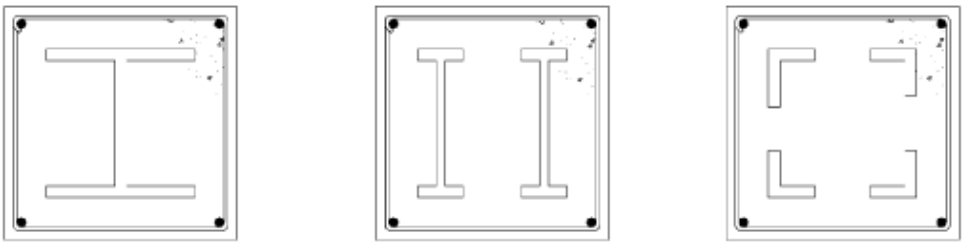

Figure 1a. Concrete-Encased Composite Columns

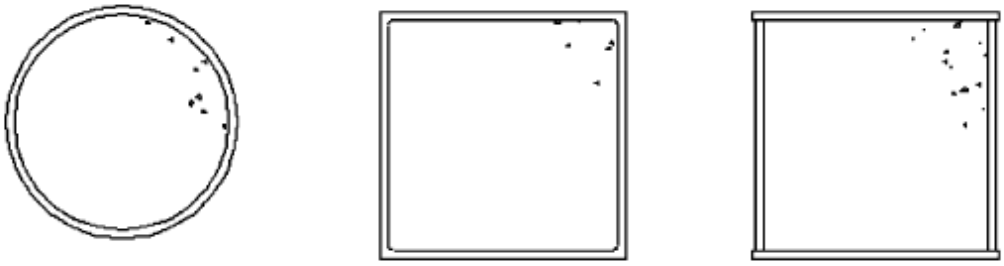

Figure 1b. Concrete-Filled Composite Columns

Figure 1. Composite Columns (Giakoumelis and Lam, 2004)

CONCRETE – FILLED STEEL TUBE (CFST) COLUMNS

Concrete – Filled Steel Tube (CFST) Column offers features better than either pure steel or reinforced concrete column due to the interaction between the external steel tube and core concrete. The strength and ductility of CFST column are increased under compression due to the effective confinement of the steel tube to the core concrete. Also, the presence of the concrete prevents the inward buckling of the steel tube and enhance the local buckling response. The steel tube acts as the formwork, and this option gives a more economical and faster construction

(Ekmekyapar and Al-Eliwi, 2016; Han *et al.*, 2014; Li *et al.*, 2015). Figure 2 shows the typical cross-sections of CFST column.

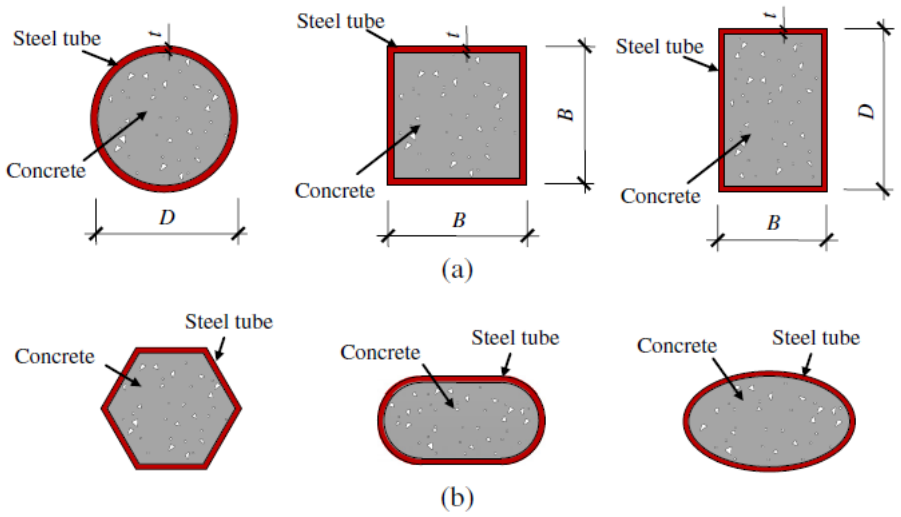

Figure 2. Typical cross – sections of CFST column (Han *et al.*, 2014)

The increase in strength, stiffness, and ductility of CFST column are provided by the confinement of steel tube to concrete core. In the early stage of loading, Poisson's ratio of concrete is lower than that of steel tube, and no confinement at this stage. When the load is increased, the Poisson's ratio of concrete increased and reach that of steel tube, core concrete expands and interacts with a steel tube to develop the passive confinement. At greater load levels, the core concrete expands laterally more than steel tube, and hence a radial pressure is developed at the interface between concrete and steel. At this stage, confinement of the concrete core is achieved, and core concrete is stressed triaxially and the steel tube biaxially (de Oliveira *et al.*, 2009; Johansson, 2002; Shanmugam and Lakshmi, 2001).
The confinement index is a parameter has been adopted to specify the confinement capability of the CFST column roughly (Han *et al.*, 2014; Han *et al.*, 2005).

$$\xi = \frac{A_s f_y}{A_c f_c} \qquad (1)$$

where A_s and A_c are the cross-sectional areas of the steel tube and core concrete, respectively, f_c is the compressive strength of concrete, and f_y is the steel yield strength.
The studies proved that the circular steel tube could provide more effective confinement to the core concrete than other types of steel tube sections. Large experimental studies focused on the performance of circular CFST column under axial load were carried out over the last decades. In addition to experimental works, several design specifications have been published to enhance the applications and design of the CFST columns.

PAST RESEARCH ON CFST COLUMNS UNDER AXIAL LOADING

Many research on circular CFST columns under axial loading has been carried out. The main parameters effect on the circular CFST column are: section slenderness ratio (diameter – to – thickness (D/t) ratio), column slenderness ratio (length – to – diameter (L/D) ratio), and materials properties which presented by concrete compressive strength f_c, and steel yield strength f_y.

Schneider (1998) studied the behavior of short concrete-filled steel tube columns under axial load experimentally. Fourteen specimens were tested to investigate the effect of the tube shape and steel tube thickness on the capacity of the columns. It was concluded that circular steel tubes offer much more post-yield axial ductility than square and rectangular tube sections.

Giakoumelis and Lam (2004) studied the effect of the steel tube thickness, the bond strength between the steel and concrete, and the confinement on the behavior of circular CFST columns with various concrete strengths under axial loading and compared the results with the predictions of the design specifications. Han *et al.* (2005) studied experimentally the behavior of self-consolidating concrete filled steel tube stub columns under axial load. The main parameters varied in the study are section type, steel yielding strength, D/t ratio. The theoretical model was used to study the influence of parameters on the ultimate strength of CFST columns. And making comparisons between the experimental results and the existing codes.

de Oliveira *et al.* (2009) studied the effect of L/D ratio and concrete strength on the confinement factor. The columns length was short and long and concrete strength normal and high strength. The capacity decreased when L/D increased, the load capacity increased for high strength concrete but the confinement improved in normal concrete strength and compared the results with some design codes.

An *et al.* (2012) investigated the behavior of very slender CFST columns. The results showed that the very slender column reaches the ultimate capacity with no confinement exist and predict the ultimate strength by design specifications.

Abed *et al.* (2013) studied the effect of D/t ratio and concrete strength of short CFST columns. The results showed the D/t ratio had a greater effect than others. when, D/t ratio increased the stiffness and axial capacity of the columns decreased due to decrease in the confinement. Also, the results compared with the current codes.

Aslani et al. (2015) Investigated the suitability of the several codes to predict the axial load capacity of high strength concrete filled steel tube columns under the axial load. According to the statistical results, simplified relationships are developed to predict the section and ultimate buckling capacities of normal and

high-strength short and slender rectangular and circular CFSTCs subjected to axial loading.

Ekmekyapar and Al-Eliwi (2016) examined the capacity and the confinement of CFST columns with three L/D ratios, two D/t ratios, three concrete compressive strength levels and two steel qualities. The results showed that the L/D ratio is very important parameter has direct impact column capacity, and D/t and confinement factor does not have a direct impact on the performance of CFST column.

AIM OF THIS STUDY

Many design specifications have been proposed to predict the axial capacity of CFST columns; the common codes are AISC360-16 (2016) and EC4 (2004) where the AISC 360 – 16 is the specification for steel structures in the United States; the EC4 is the European code for composite structure design. The aim of this study is to confirm the applicability and prediction of AISC 360 – 16 and EC4 codes for circular CFST columns under axial loading and compare them.

STRENGTH PREDICTION OF CIRCULAR CFST COLUMNS

The AISC 360 – 16 and EC4 codes depend on different functions to estimate the axial load capacity of CFST columns. These codes have some limitations on geometrical properties of the steel tube, and materials properties of steel and concrete and these limitations are different according to the code. Table 1 shows the limitations of these design specifications.

Table 1. Limitations of Design Specifications

Parameter	AISC 360 – 16	EC4
f_y (MPa)	$f_y \leq 525$	$235 \leq f_y \leq 460$
f_c of NW (MPa)	$21 \leq f_c \leq 70$	$20 \leq f_c \leq 60$
D/t	$\leq 0.31\,(E_s/f_y)$	$\leq 90\,(235/f_y)$
Steel amount	$\geq 1\%$ of gross area	$0.2 \leq \delta \leq 0.9$
Slenderness	$KL/r \leq 200$	$\lambda \leq 2$

Where E_s refers the elastic modulus of the steel tube, K is the effective length factor based on end boundary conditions of the column, λ refers the relative slenderness and, δ is the steel contribution ratio defined in EC4:

$$\delta = \sqrt{\frac{A_s f_y}{N_{pl.Rd}}} \qquad (2)$$

Elastic modulus of the concrete, E_c, is calculated in each specification as presented in Table 2.

Table 2. Elastic Modulus of the Concrete

Specification	E_c (MPa)	Details
AISC 360-16	$0.043 w_c^{1.5} \sqrt{f_c}$	w_c: Concrete density ($1500 \leq w_c \leq 2500\ kg/m^3$).
EC4	$22000\ ((f_c + 8)/10)^{0.3}$	

AISC 360 – 16

The nominal strength of composite sections shall be determined by the plastic stress distribution method, where the steel tube reaches the yield stress f_y when the core concrete strength about $0.95f_c$. The CFST sections are classified as compact, noncompact or slender. This classification accordance to the cross-section slenderness (D/t) ratio. The section is compact if the D/t ratio does not exceed $\lambda_p = 0.15E/f_y$, noncompact if the D/t ratio exceed λ_p but does not exceed $\lambda_r = 0.19E/f_y$, and slender if the D/t ratio exceeds λ_r. For all cases, the maximum D/t ratio does not exceed $0.31E/f_y$.

The nominal compressive strength of doubly symmetric axially loaded CFST shall be determined for the limit state of flexural buckling based on member slenderness as follows:

$$P_{AISC} = P_{no}\left[0.658^{\frac{P_{no}}{P_e}}\right] \qquad \frac{P_{no}}{P_e} \leq 2.25 \qquad (3)$$

$$P_{AISC} = 0.877 P_e \qquad \frac{P_{no}}{P_e} > 2.25 \qquad (4)$$

Where, P_{no} is the nominal strength of the composite section and P_e is the Euler critical load, which is calculated using effective stiffness $(EI)_e$:

$$(EI)_e = E_s I_s + C_3 E_c I_c \qquad (5)$$

$$P_e = \frac{\pi^2 (EI)_e}{(KL)^2} \qquad (6)$$

$K = 1$

C_3 is the coefficient of effective rigidity of the CFST column:

$$C_3 = 0.45 + 3\left(\frac{A_s}{A_s + A_c}\right) \leq 0.9 \qquad (7)$$

For compact section, the nominal axial capacity is calculated as:

$$P_{no} = P_p \qquad (8)$$

$$P_p = A_s f_y + C_2 A_c f_c \quad (9)$$

Where, P_p is the plastic strength of the section, $C_2 = 0.95$, a circular section.
AISC 360 – 16 adopts the confinement effect of circular section by the coefficient of C_2 of 0.95, which gives an 11% constant improvement due to confinement.

For non – compact section; the nominal axial capacity is evaluated as:

$$P_{no} = P_p - \frac{P_p - P_y}{(\lambda_r - \lambda_p)^2}(\lambda - \lambda_p)^2 \quad (10)$$

$$P_y = A_s f_y + 0.7 A_c f_c \quad (11)$$

Where, P_y is the yield strength of the composite section.

For slender section, the nominal axial capacity is given by:

$$P_{no} = A_s f_{cr} + 0.7 A_c f_c \quad (12)$$

$$f_{cr} = \frac{0.72 f_y}{\left(\left(\frac{D}{t}\right)\frac{f_y}{E_s}\right)^{0.2}} \quad (13)$$

f_{cr} is the critical local buckling stress of the filled circular section.

EC4

EC4 code adopts simplified method to predict the capacity of CFST columns. This code gives details to estimate the confinement effect, and the confinement effect is considered if the relative slenderness ($\bar{\lambda}$) is lower than 0.5. The plastic resistance of the CFST section ($N_{pl.Rd}$) is calculated by adding the resistance of the steel and concrete. The plastic compressive capacity of circular CFST column as:

$$N_{EC4} = \eta_a A_s f_y + A_c f_c \left(1 + \eta_c \frac{t}{D}\frac{f_y}{f_c}\right) \quad (14)$$

Where, η_a is the steel reduction factor, where the yield stress decreased due to the hoop stress. And η_c is the concrete enhancement factor, where, the concrete strength increased under triaxial stress state.
when eccentricity is smaller than 10% of the outer diameter of the steel tube D, the steel reduction and the concrete enhancement factors are evaluated as follows:

$$\eta_a = 0.25(3 + 2\bar{\lambda}) \leq 1.0 \quad (15)$$

$$\eta_c = 4.9 - 18.5\bar{\lambda} + 17\bar{\lambda}^2 \geq 0 \quad (16)$$

$\bar{\lambda}$: the relative slenderness ratio; the confinement effect is considered, if the value of $\bar{\lambda}$ does not exceed 0.5.

$$\bar{\lambda} = \sqrt{\frac{N_{pl.Rd}}{N_{cr}}} \leq 0.5 \quad (17)$$

Where, $N_{pl.Rd}$ is the plastic resistance of column, and N_{cr} is the Euler critical load:

$$N_{pl.Rd} = A_s f_y + A_c f_c \quad (18)$$

$$N_{cr} = \frac{\pi^2 (EI)_e}{(KL)^2} \quad (19)$$

Where, $(EI)_e$ is the effective stiffness of the member which is given by:

$$(EI)_e = E_s I_s + K_e E_c I_c \quad (20)$$

Where, E_s; E_c are the elastic modulus of steel and concrete, respectively. Table 2 defines the modulus of elasticity of concrete. I_s; I_c are the moment of inertia of steel tube section and concrete section, respectively. Finally, K_e is a correction factor equal to 0.6.

EC4 considered the effect of imperfections that might be caused second order moments by multiplying the column plastic resistance by a reduction factor χ:

$$\chi = \frac{1}{\phi + \left(\phi^2 - \bar{\lambda}^2\right)^{0.5}} \leq 1.0 \quad (21)$$

The reduction factor χ is calculated using European column curves and the parameter ϕ is calculated as:

$$\phi = 0.5\left[1 + \alpha\left(\bar{\lambda} - 2\right) + \bar{\lambda}^2\right] \quad (22)$$

Where, α is an imperfection factor, equal to 0.21 for circular CFST columns.

PARAMETRIC STUDY OF CIRCULAR CFST COLUMNS

This study aims to investigate the appropriateness of AISC 360 – 16 and EC4 of practice for predicting the capacity of circular CFST columns under axial loading, where the data will be within and behind the limitations of these codes and analyze the results, where the variation of geometrical and material properties covered in this study. A total of 81 specimens, where various structural

parameters were varied to investigate their combined effect: concrete compressive strength f_c taken as 20, 60, and 100 MPa to cover normal and high strength concrete, steel tube yield strength f_y taken as 235, 435, and 600 MPa to cover mild and high tensile strength steel, D/t ratio taken as 20, 60, and 100, and L/D ratio taken as 3, 6, and 9 to cover short and long columns.

In definition of short and long CFST columns the AISC 360 – 16 and EC4 codes are completely different, therefore, the term "short column" and "long column" are classified according to L/D ratio, where the "short column" is defined as specimen with L/D ratio less than or equal 4, while, "long column" is defined as specimen with L/D ratio more than 4 (Han *et al.*, 2014; Le Hoang and Fehling, 2017; Li *et al.*, 2015). The modulus of elasticity of steel tube is 200 GPa, and modulus of elasticity of concrete is determined according to the corresponding codes.

The effect of parameters on axial capacity of CFST columns

To study the behavior of the CFST columns, there are materials and geometrical parameters are effect on the axial capacity of column, (1) concrete compressive strength f_c, (2) steel tube yield strength f_y, (3) diameter – to – thickness D/t ratio, and (4) length – to – diameter L/D ratio.

To investigate which parameter has more effect on the axial capacity of the CFST column, the results of analysis of variance by using Minitab software showed that the D/t ratio and concrete compressive strength have the more effects than other parameters and the maximum interaction is between D/t ratio and f_y for both AISC 360 – 16 and EC4.

The results show that the CFST column of (D/t = 20, L/D = 3, f_c = 100 MPa, and f_y = 600 MPa) gives the maximum axial capacity of 7.501 MN, and 9.063 MN for both AISC 360 – 16 and EC4 respectively by difference about 20.8% where the EC4 takes the confinement effect on its consideration. While the CFST column of (D/t = 100, L/D = 9, f_c = 20 MPa, and f_y = 235 MPa) gives the minimum axial capacity of 1.034 MN, and 1.117 MN for both AISC 360 – 16 and EC4 respectively by difference about 8%.

Figure 4 and Figure 5 present the interaction plots for both AISC 360 – 16 and EC4. Use an interaction plots to show how the relationship between one parameter and the mean of the axial capacity depends on the value of the second parameter.

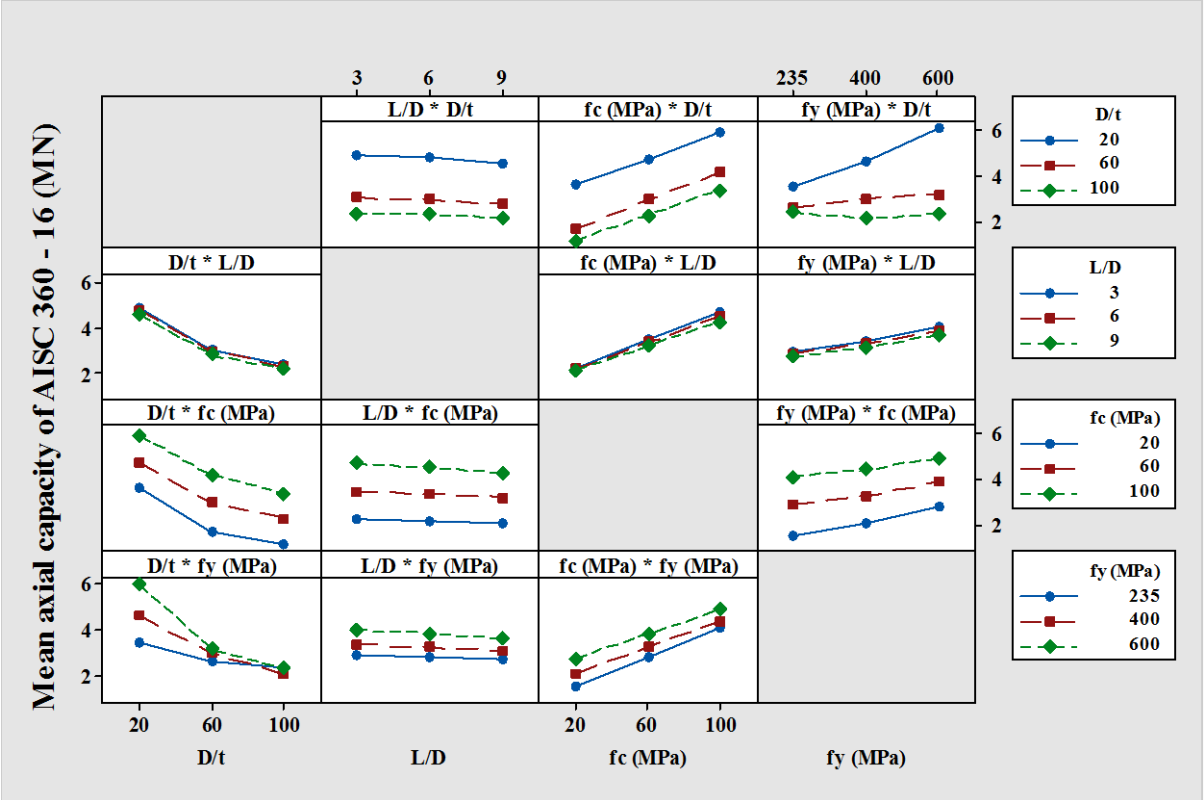

Figure 4. Interaction Plot of AISC 360 – 16 Design Code

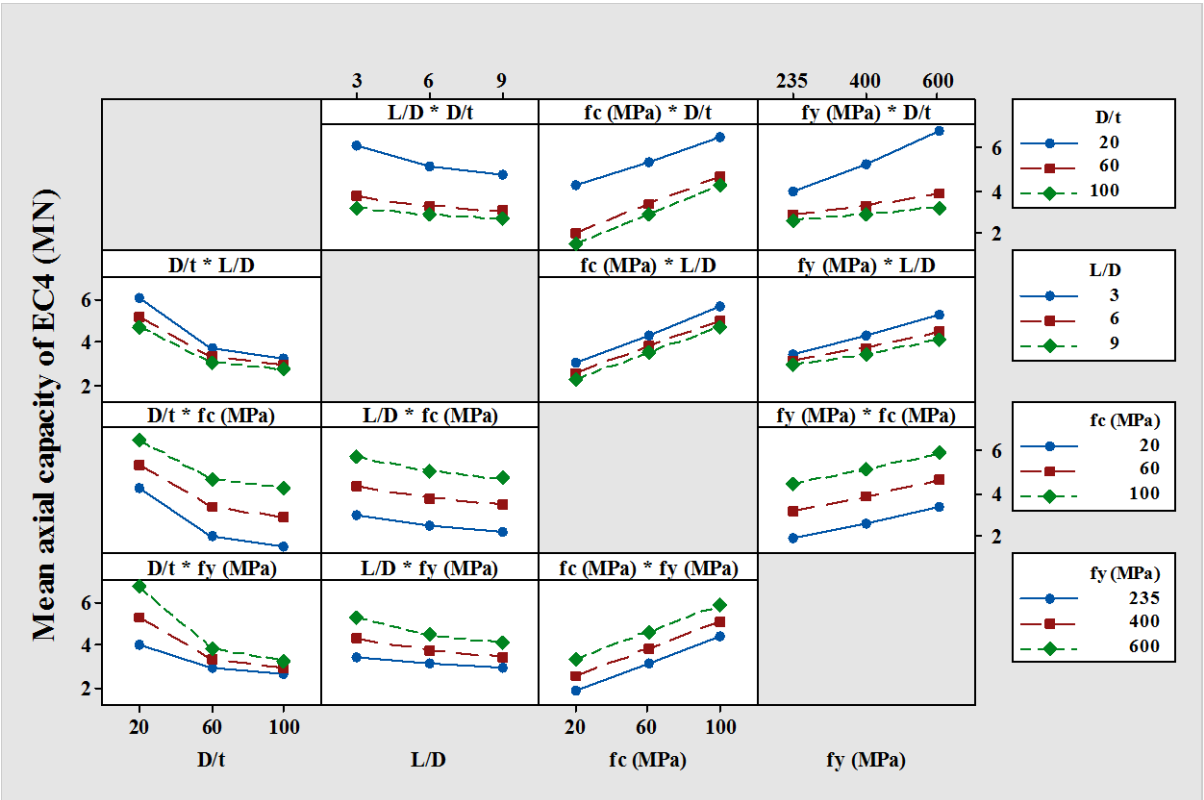

Figure 5. Interaction Plot of EC4 Design Code

Effect of concrete compressive strength f_c

The effect of concrete compressive strength f_c is shown in Figure 6 for both AISC 360 – 16 and EC4, where the axial capacity increase when f_c increases.

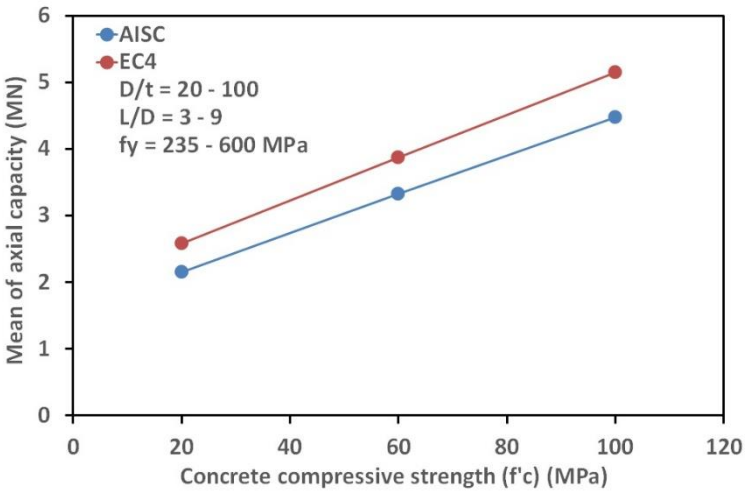

Figure 6. Effect of f_c on Axial Capacity of CFST Columns

This increasing in axial capacity of the CFST columns is due to the effects of confining tube in increasing the infill concrete compressive strength f_c. As shown in Figures 4 and 5, the maximum axial capacity gives when f_c = 100 MPa with D/t = 20 compared with others parameters.

Effect of steel yield strength f_y

Figure 7 shows the influence of f_y, for both AISC 360 – 16 and EC4 the axial capacity of the CFST column increase when increase in f_y increases. Figures 4 and 5 present the maximum axial capacity gives when f_y = 600 MPa with D/t = 20 compared with others parameters.

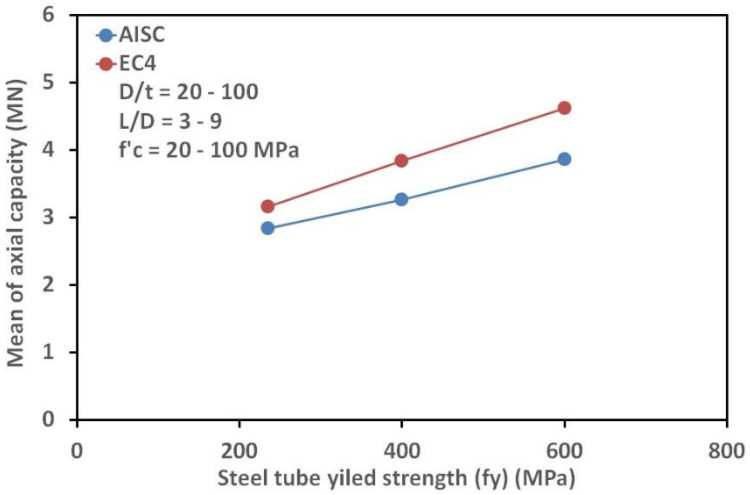

Figure 7. Effect of f_y on Axial Capacity of CFST Columns

Effect of diameter – to – thickness D/t ratio

D/t ratio also defines as cross-section slenderness ratio also this ratio effect on local buckling of the CFST columns, however, the for AISC 360 – 16 the local buckling accounted according to the classification of cross-section as compact, noncompact and slender. While the EC4 the local buckling occurs when this ratio passed the maximum value. Furthermore, this parameter effect on the confinement as shown in Equation 1. For both AISC 360 – 16 and EC4 the axial capacity of the CFST column decrease when D/t increases due to the reduction in confinement provided by small thickness. Figure 8 shows the influence of D/t ratios on the axial capacity of the CFST columns. However, the D/t = 20 gives the maximum effect with compared with other values (D/t = 60, 100).

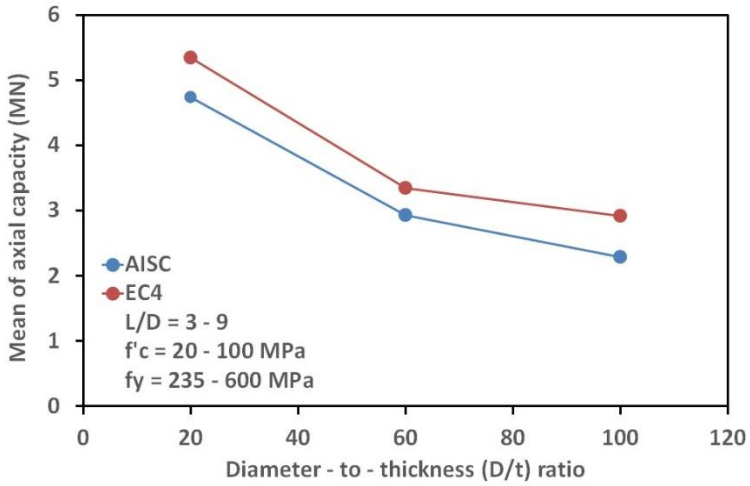

Figure 8. Mean Effect Plot of D/t Ratio

Effect of length – to – diameter L/D ratio

The L/D ratio affects the axial capacity and the confinement effect of the CFST columns, where, both decrease when L/D ratio increased (de Oliveira *et al.*, 2009; Ekmekyapar and Al-Eliwi, 2016). Figure 9 shows the mean effect of L/D ratio on the axial capacity of the CFST columns for both AISC 360 – 16 and EC4. Where the axial capacity of short columns (L/D = 3) greater than long columns (L/D =6 and 9). Also from Figures 4 and 5 the L/D = 3 with D/t ratio = 20 gives the maximum axial capacity in compared with other parameters.

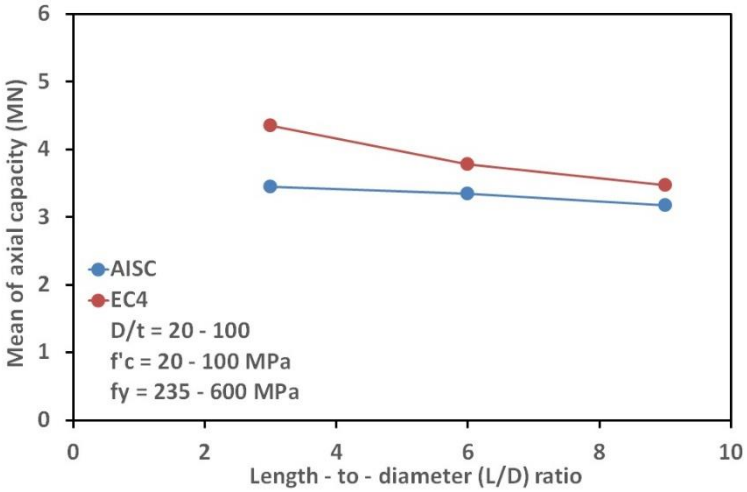

Figure 9. Mean Effect Plot of L/D Ratio

The strength index (SI) and the confinement index (ξ)

For the design of the CFST columns, most codes recognize the effect of the "composite action" especially for members with the circular cross – section. Therefore, the strength of the composite member is enhanced. Strength index *SI* and the confinement index ξ are very useful measures for composite action and confinement assessments in CFST columns. where ξ is defined in equation 1 and *SI* is defined as follows and (Ekmekyapar and Al-Eliwi, 2016; Han *et al.*, 2014; Portolés *et al.*, 2011; Yang *et al.*, 2008; Yu *et al.*, 2008):

$$SI = \frac{P_u}{P_{uo}} \quad (23)$$

Where, P_u is the axial capacity of a CFST column predicted by AISC 360 – 16 and EC4 codes. And P_{uo} is the sectional capacity or sqush load:

$$P_{uo} = A_s f_y + 0.85 A_c f_c \quad (24)$$

The following Figures 10 to 13 show the effect of parameters of the parametric study on the strength index. For AISC 360 – 16 *SI* ranges from 0.747 to 1.088 and

for EC4 ranges from 0.937 to 1.403 by increasing in mean about 18%, this in difference is due to the EC4 code take the confinement effect in its consideration. Figures 10 and 11 show that *SI* for normal strength concrete (f_c = 20 MPa) greater than high strength concrete (60 and 100 MPa) and for mild steel strength (f_y = 235 MPa) gretaer than higher strength steel strength (400 and 600 MPa) because the squash load of the CFST column depends on cross – section and the materials properties f_c and f_y.

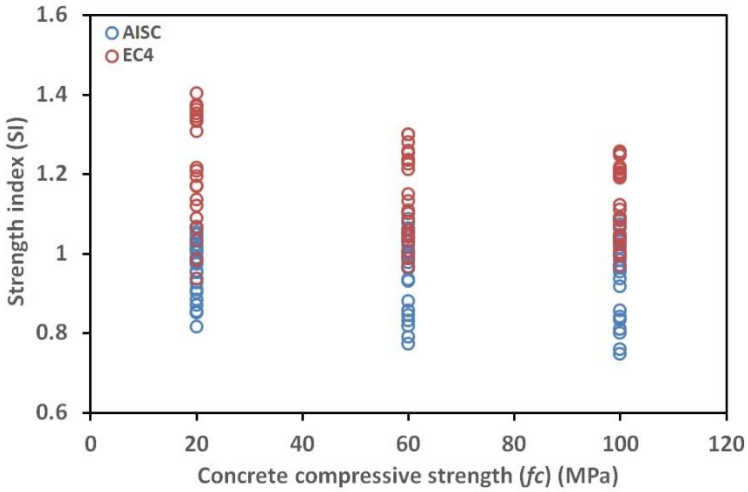

Figure 10. Effect of f_c on the Strength Index *SI*

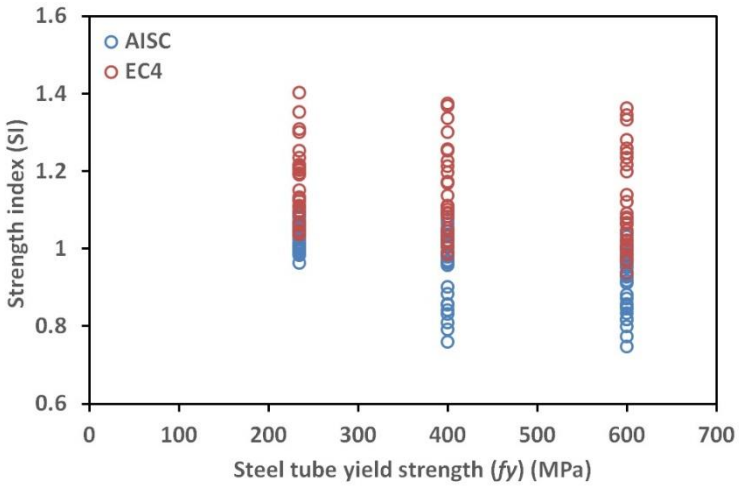

Figure 11. Effect of f_y on the Strength Index *SI*

Figure 12 shows the effect of D/t ratio on the strength index for both AISC 360 – 16 and EC4 codes. The strength index decreased when the D/t ratio increases this means the thicker tube provides confinement more than, the thinner tube. The column's ductility decreases as the concrete compressive strength increases for higher D/t ratios, but for smaller D/t ratios the opposite is true (Abed *et al.*, 2013).

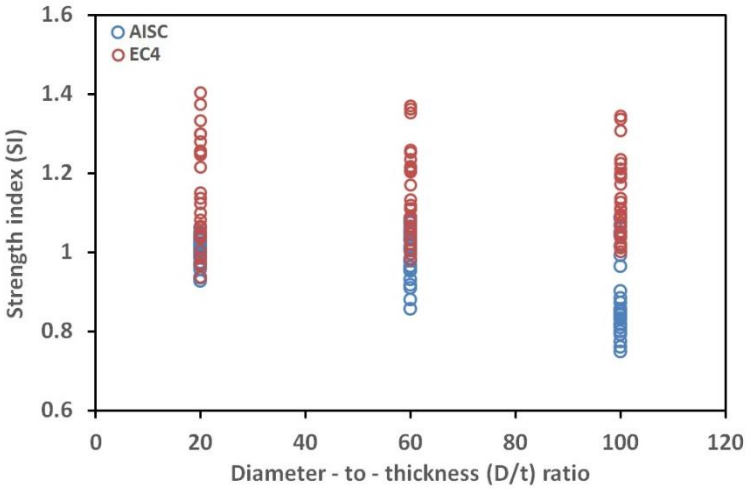

Figure 12. Effect of D/t Ratio on the Strength Index *SI*

As shown in Figure 9, the L/D ratio has a direct impact on the axial capacity of the CFST column. The short columns have an axial capacity greater than long columns for both AISC 360 – 16 and EC4. This also clear in Figure 13 where the short columns have strength index more than unity particularly for EC4 due to the effect of the L/D ratio on the confinement index, where the confinement decrease when L/D ratio increases. For a column with small L/D ratio, the failure is recognized by material yielding while for high L/D ratio the failure is characterized by global instability with small deformation before the facing the confinement (de Oliveira *et al.*, 2009).

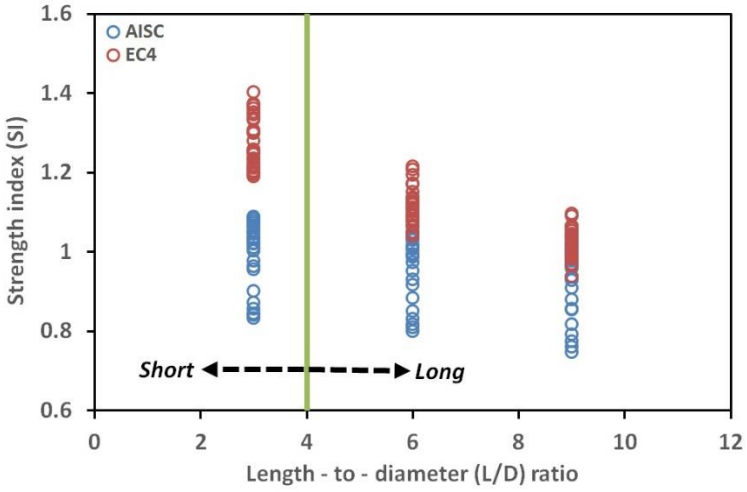

Figure 13. Effect of L/D ratio on the Strength Index *SI*

The confinement index ξ is a function of D/t ratio, as well as the material properties f_c and f_y, for this parametric study the confinement index ranges from 0.097 to 7.037. Figures 14 – 16 show the relation between the D/t ratios and the confinement index ξ with different values of f_c and f_y. It is observed that the samples of D/t ratios = 20 with f_c = 20 MPa and f_y = 600 MPa are more affected on the confinement index.

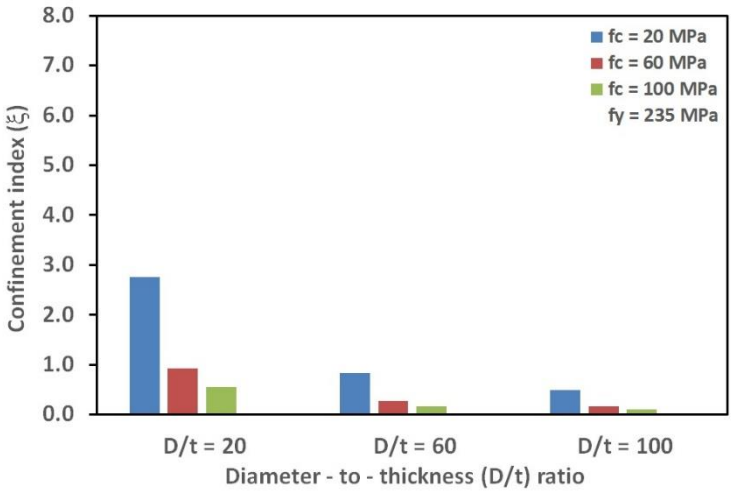

Figure 14. D/t Ratio Versus the Confinement Index ξ, f_y = 235 MPa

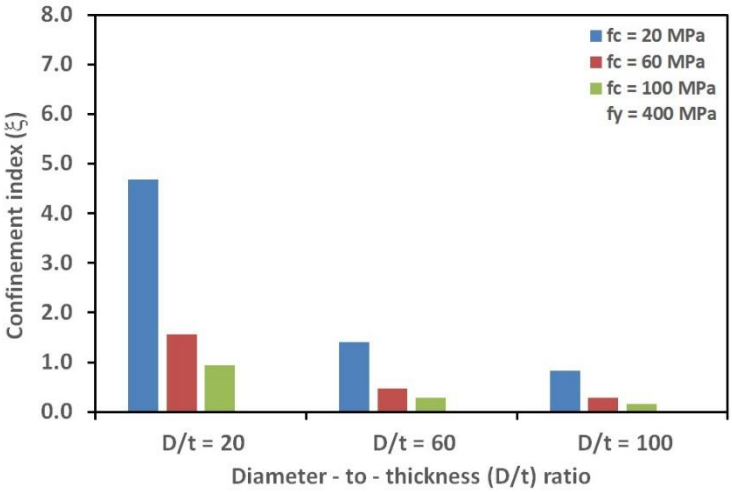

Figure 15. D/t Ratio Versus the Confinement Index ξ, f_y = 400 MPa

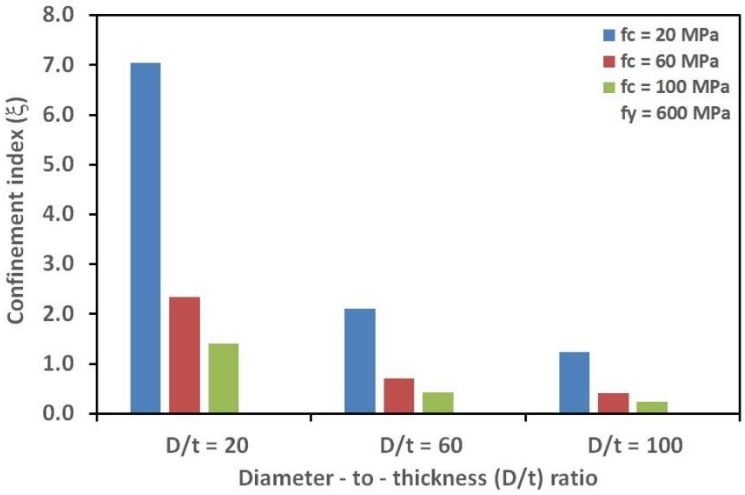

Figure 16. D/t Ratio Versus the Confinement Index ξ, f_y = 600 MPa

As a summary of this parametric study, Table 3 shows the difference in predictions between AISC 360 – 16 and EC4, where, the percentage of the difference of the axial capacity for total columns specimens is 16.53%, this difference due to the confinement effect and the variation between the limitations of codes for materials and geometrical properties, when classify the columns specimens according to length, the difference is 26.24% this exactly due due to the confinement where EC4 takes in its consideration the confinement effect for short column while for long columns the difference decreased to 11.39% because no confinement effect for long column in EC4 calculations.

Also for the same reasons the same result is clear to observe for strength index calculations for short and long columns where the difference is 27.83% and 12.95% respectively. For normal strength concrete (NSC) and high-strength concrete (HSC), also the variation is clear for prediction of axial capacity between two codes, generally, the confinement is more effective when the infilled concrete is NSC due to its higher deformation capacity in comparison with the HSC (de Oliveira *et al.*, 2009), this result is obvious in mean of SI_{EC4} between NSC and HSC due to confinement effect while it is slight difference in SI_{AISC} because no big effect of confinement in this code.

The same conclusion observed when comparisons between the mean of the confinement index ξ between NSC and HSC. While there is no effect of length on the mean of ξ because the equation 1 do not take the length in calculations. conversely for steel tube strength, where, the mild steel strength (MSS) ($f_y \leq 460$ MPa) gives lower confinement than high tensile steel strength (HSS) ($f_y > 460$ MPa).

Table 3. Summary of the Results

	Mean of P_{AISC} (MN)	Mean of P_{EC4} (MN)	P_{EC4}/P_{AISC} (%)	Mean of SI_{AISC}	Mean of SI_{EC4}	SI_{EC4}/SI_{AISC} (%)	Mean of ξ
Total columns	3.321	3.870	16.53	0.964	1.139	18.09	1.213
Short columns	3.447	4.351	26.24	0.999	1.276	27.83	1.213
Long columns	3.258	3.630	11.39	0.947	1.070	12.95	1.213
NSC	2.211	3.010	36.09	0.994	1.354	36.20	2.374
HSC	4.064	5.022	23.56	1.001	1.238	23.67	0.633
MSS	3.051	3.498	14.639	0.993	1.151	15.94	0.936
HSS	3.861	4.615	19.518	0.908	1.115	22.79	1.768

CONCLUSIONS

The present study is an attempt to compare between the prediction of AISC 360 – 16 and EC4 of composite columns, with the rapid growth of research and application of concrete-filled steel tube in the world, the circular concrete-filled steel tube column under axial loading is considered as a parametric study. On the basis of this study, the following conclusions can be drawn:

The variation of geometrical and material properties of specimens suggested covering the practical cases in this field.
These specimens were within and behind the limitations of the AISC 360 – 16 and EC4 codes.
The AISC 360 – 16 and EC4 codes depend on different functions to estimate the axial load capacity of CFST columns. Therefore, there is the difference in results between them.
The EC4 takes the confinement effect within its consideration that represents by the term $\left(1+\eta_c \frac{t}{D}\frac{f_y}{f_c}\right)$ as shown in equation 14, while for AISC 360 – 16 is constant as shown in equation 9.
The parameters of geometrical and material properties of specimens are the effect on the predictions of both codes with different percentages.
The analysis of variance showed that the D/t ratios and f_c have the more effective parameters than others and the maximum interaction occurred for D/t ratio and f_y.
The CFST column of (D/t = 20, L/D = 3, f_c= 100 MPa, and f_y = 600 MPa) gives the maximum axial capacity for AISC 360 – 16 and EC4 respectively by difference about 20.8% where the EC4 takes the confinement effect on its consideration.

While the CFST column of (D/t = 100, L/D = 9, f_c = 20 MPa, and f_y = 235 MPa) gives the minimum axial capacity for AISC 360 – 16 and EC4 respectively by difference about 8%.
The axial capacity increased when f_c and f_y increase, while decreased when D/t ratio and L/D ratio increase.
Strength index *SI* and confinement index ξ are very useful measures for composite action and confinement assessments in CFST columns. *SI* for NSC and short column is greater than HSC and long column, while the HSS gives confinement index more than MSS.

REFERENCES

Abed, F., AlHamaydeh, M., and Abdalla, S. (2013). Experimental and numerical investigations of the compressive behavior of concrete filled steel tubes (CFSTs). *Journal of Constructional Steel Research, 80*, 429-439. doi: 10.1016/j.jcsr.2012.10.005
AISC360-16. (2016). ANSI/AISC 360-16 Specification for Structural Steel Buildings (pp. 676). Chicago, Illinois, USA: American institute of steel construction.
An, Y.-F., Han, L.-H., and Zhao, X.-L. (2012). Behaviour and design calculations on very slender thin-walled CFST columns. *Thin-Walled Structures, 53*, 161-175. doi: 10.1016/j.tws.2012.01.011
Aslani, F., Uy, B., Tao, Z., and Mashiri, F. (2015). Predicting the axial load capacity of high-strength concrete filled steel tubular columns. *Steel and Composite Structures, 19*(4), 967-993. doi: 10.12989/scs.2015.19.4.967
de Oliveira, W. L. A., De Nardin, S., de Cresce El Debs, A. L. H., and El Debs, M. K. (2009). Influence of concrete strength and length/diameter on the axial capacity of CFT columns. *Journal of Constructional Steel Research, 65*(12), 2103-2110. doi: 10.1016/j.jcsr.2009.07.004
EC4. (2004). EN1994-1-1Eurocode4. DesignofCompositeSteelandConcreteStructures-Part 1-1:General Rules and Rules for Buildings (pp. 117). CEN, Brussels: European Committee for Standardization.
Ekmekyapar, T., and Al-Eliwi, B. J. M. (2016). Experimental behaviour of circular concrete filled steel tube columns and design specifications. *Thin-Walled Structures, 105*, 220-230. doi: 10.1016/j.tws.2016.04.004
Giakoumelis, G., and Lam, D. (2004). Axial capacity of circular concrete-filled tube columns. *Journal of Constructional Steel Research, 60*(7), 1049-1068. doi: 10.1016/j.jcsr.2003.10.001
Han, L.-H., Li, W., and Bjorhovde, R. (2014). Developments and advanced applications of concrete-filled steel tubular (CFST) structures: Members. *Journal of Constructional Steel Research, 100*, 211-228. doi: 10.1016/j.jcsr.2014.04.016
Han, L.-H., Yao, G.-H., and Zhao, X.-L. (2005). Tests and calculations for hollow structural steel (HSS) stub columns filled with self-consolidating concrete (SCC). *Journal of Constructional Steel Research, 61*(9), 1241-1269. doi: 10.1016/j.jcsr.2005.01.004

Johansson, M. (2002). The efficiency of passive confinement in CFT columns. *Steel and Composite Structures, 2*(5), 379-396. doi: 10.12989/scs.2002.2.5.379
Le Hoang, A., and Fehling, E. (2017). Numerical study of circular steel tube confined concrete (STCC) stub columns. *Journal of Constructional Steel Research, 136*, 238-255. doi: 10.1016/j.jcsr.2017.05.020
Li, N., Lu, Y.-Y., Li, S., and Liang, H.-J. (2015). Statistical-based evaluation of design codes for circular concrete-filled steel tube columns. *Steel and Composite Structures, 18*(2), 519-546. doi: 10.12989/scs.2015.18.2.519
Liang, Q. Q. (2014). *Analysis and Design of Steel and Composite Structures*: CRC Press.
Portolés, J. M., Romero, M. L., Bonet, J. L., and Filippou, F. C. (2011). Experimental study of high strength concrete-filled circular tubular columns under eccentric loading. *Journal of Constructional Steel Research, 67*(4), 623-633. doi: 10.1016/j.jcsr.2010.11.017
Schneider, S. P. (1998). Axially loaded concrete-filled steel tubes. *Journal of Structural Engineering, ASCE 124*(10), 1125-1138.
Shanmugam, N., and Lakshmi, B. (2001). State of the art report on steel–concrete composite columns. *Journal of Constructional Steel Research, 57*(10), 1041-1080.
Yang, H., Lam, D., and Gardner, L. (2008). Testing and analysis of concrete-filled elliptical hollow sections. *Engineering Structures, 30*(12), 3771-3781. doi: 10.1016/j.engstruct.2008.07.004
Yu, Q., Tao, Z., and Wu, Y.-X. (2008). Experimental behaviour of high performance concrete-filled steel tubular columns. *Thin-Walled Structures, 46*(4), 362-370. doi: 10.1016/j.tws.2007.10.001

DEVELOPMENT OF REMOTE CONTROLLABLE POWER STRIP FOR HOME ENERGY MANAGEMENT THROUGH WEB-SERVICES

Aymen Husam ALADHAMİ
aymen.aladhami@yahoo.com
University of Gaziantep, Dept. of Electrical
Electronics Eng. , Gaziantep Turkey

Ergun ERÇELEBİ
ergun.ercelebi@gmail.com
University of Gaziantep, Dept. of Electrical
Electronics Eng. , Gaziantep Turkey

ABSTRACT: In the paper, we have presented development of power strip for management of home power to reduce standby power consumption. The developed power strip integrates many hardware components as AC power socket, XBee module have been used to make communications between central control unit and power strip. Raspberry pi card configured to play the role as a web server and coordinator to switch ON/OFF strip power and measure power consumption of plugged home appliances that collected from power sensor using XBee module. Also, software has been developed using HTML, PHP, Javascript and Phyton to design web page as platform compatible with any internet browser in any smart phone or personal computer. However, our development requires static IP number. We have evaluated in our design under different conditions. We have found the results are satisfactory.

Key words: power strip, Xbee, Rapberry Pi, web server.

INTRODUCTION

Technology has become an integrated part of people's lives and the internet has become a common interface that many devices use for simplify the daily life of people (Pavithra & Balakrishnan, 2015). Access to the Internet is very easy through smart phones and tablets. Smart power strip developed to provide technical solution to meet the comfort needs and energy management (HAN, LEE, & PARK, 2009).

Remote controllable and energy saving room architecture for periodically monitor the power consumption via ZigBee controller with IR code learning functionality, user can control the power outlet and the dimming light. With the advent of mobile phones containing techniques including Bluetooth as well Short Message Service (SMS), Allow to implement home power management, and develop controllable power socket based on microcontroller (LIEN, BAI, & LIN, 2007).

In the same context it was developed platform of smart homes to customize java-based application development platform (JADP) in mobile phone as a result it could be more flexible remote debugger and easy to develop (Chen & Chen, 2008).

Energy management system (EMU) developed based on Wireless Sensor Network (WSN) using XBee-pro ZigBee, Arduino Uno microcontroller and current sensor (ACS712) for control energy consumption and monitor the system in real-time using NILABVEW software, ThingSpeak Website used as Cloud for storing and display sensor data (Abo-Zahhad & Ali, 2015).

The main contribution of this paper is to implement an electronic card which can control household equipment such as television, light and etc., through the internet under any operating system environment. The platform consists of develop programs that allow communication between a remote user and household network.

User can remotely unplug household devices when they are not being used. Wherefore we have developed Remote controllable power strip based on XBee wireless module and minicomputer (Raspberry pi) to allow homeowners to control and monitor power usage of home appliances.

System Architecture

Generally smart power strip architecture consists of three main components (Lamine & Abid, 2014): Central Control Unit, power socket and Communication protocol.
Central Control Unit is the gateway between user and power strip, our development based on Raspberry Pi3 card. The power socket provides the interface between the developed home energy management and the non-smart load appliances in real time. The power socket is designed to provide remote control of non-smart loads thus providing a practical solution to interface the loads with the developed system and schedule on/off status of selected loads. The power socket is responsible for collecting data about the environment around it and sending that data to processor in the network which is measure the power consumption of the different loads and transfer it to the Central Control Unit. Communication protocol; there are many Smart Home Communication Technologies in the market most popular is (X10, Z-Wave, ZigBee, INSTONE, EnOccean) (Withanage & Otto, 2014). The most relevant communication technologies used in smart home systems ZigBee protocol.

Raspberry pi

We used Raspberry Pi3 shown in figure 1. that contains built in 802.11n Wireless LAN that get more flexible and movable anywhere user want to put it, In our development Raspberry Pi will be mediator between user and power strip that

connect to home appliances, the Raspberry Pi is used as the gateway which communicates to personal computer or smartphone using http protocol.

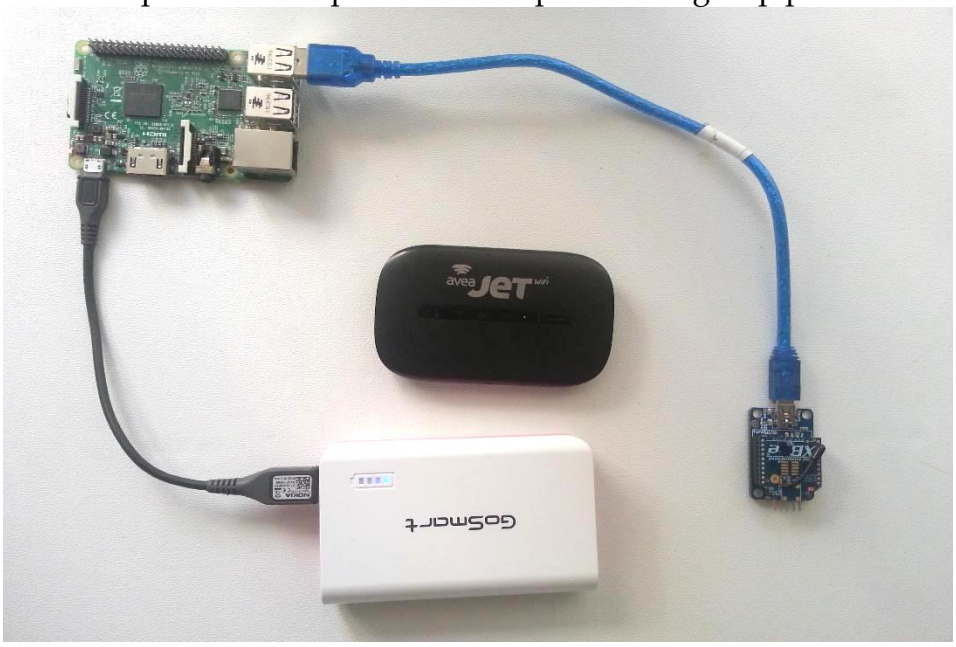

Figure 1: Central Control Unit using Raspberry Pi-3

Web server

Raspberry Pi can be connected to the Router and Internet through wireless LAN and Rj45. One of its configuration Features is to work as a web-server. There are many alternative web servers that may be installing on the raspberry Pi, like Apache and NGINX (raspberrypi, 2017). Apache is a popular web server application the user can install on the Raspberry Pi to allow it to serve web pages. Apache can serve HTML files over HTTP and with additional modules can serve dynamic web pages using scripting languages such as PHP.

There are a new breed tools that reach programming languages like python, JavaScript and Cascading Style Sheets (CSS) to make web server dynamically generate the hypertext markup language. Web page consists of three main components: First is buttons for turn ON/OFF that programmed using JavaScript that call PHP code for calling python script that send digital signals over ZigBee technology to the node. The second component is label text. It is also developed based on Java-PHP which is able to get data stream without any reload page from the database. The Chart is the third component the in web page, Interactive JavaScript charts (highcharts) provides many types of charts and has many advantages, dynamic chart (Spline updating each second) has been used, fetching sensor data that stored in the database with date and time at the moment of reading.

Database

Install MySQL-server database and then the php5-mysql install adds the MySQL libraries to allow PHP to access the MySQL database.
The database that we created include one table and five Columns:

Id: AUTO_INCREMENT attribute can be used to generate a unique identity for new rows.
Current date: date and time at the sensing moment.
Current data: sensing value after making mathematical processing to get Electric current.
Power data: Electric power in Watt.
Status: There are four status cases, status column It contain one of these values (0,1,2,3) as below:
Status = 0: ZigBee Not connected.
Status = 1: No data or Power strip if off.
Status = 2: error data received.
Status = 3: Power strip is ON.

XBee module

The advantages of this module is too small size as a coin and with low power usage. The XBee module communication concepts have either point-to-point or star communication concept. [11]
In addition, it is compatible with many minicomputers and boards, Since a USB port feasible with XBee, there are 11 digital I/O pins and 4 analog input pins in ZigBee. The XBee is linked to Raspberry Pi via USB working in coordinator mode and the other XBee is the End point mode. The pin-20- (DIO0) is set as digital output to control relay to turn ON/OFF, Pin-19- (AD0) is set to work as analog to digital converter which is connected to current sensor (ASC712) and convert the voltage (analog data) coming from V-out of sensor and send it to coordinator as a stream of digital data every 0.5 second.

Power strip hardware

The most important features of the power outlet development is to be simple and uncomplicated. It affects the cost, power consumption and easy to understand.
The transformer steps down the main voltage from 220 V AC to 5 V DC to provide voltage to the electromechanical relay and current sensor. The 5 V to 3.3 V is to provide XBee wireless module with power.

Additionally, the current sensor signal output is connected to the XBee pin-19- (AD1). The analog to digital converter (ADC) of each XBee module has a resolution conversion of 10 bit.

Hall-Effect-Based Linear Current Sensor type ACS712 ±5 A is used and the output is connected to an operational amplifier (op-amp) based signal conditioning circuit so as to read the required analog values to the pins of the analog input of the XBee module (sparkfun, 2017). The (op-amp) IC circuit is used for the conversion from AC to root mean square (RMS) signal and to shift ACS712 sensor zero current from 2.5 V to 0 V . Since the XBee has a built in 10-bits analog-to-digital converter ADC; therefore 10 bits = 1024 steps (0–1023). So the step size using XBee s1 Vref = (3.3 V) then the equation will be (3.3V/1024 = 3.223 mV/step) (Ahmed & Ali, 2017).

ACS712 ±5 A 185 mV/A output sensitivity, 100 mV/A for ±20 A, and 66 mV/A for ±30 A, sensor Vout data range between 1.5-3.5 V as the datasheet.
So the form of the equation will be: Current = (((3.3 / 1024) * (Vout)) / (0.185*2)).

Hardware implementation and experiment

The implementation of this work starts with selecting the operating system that we prefer. In this project we have selected raspbian operating system. Now, we have to boot the operating system that we have selected with the necessary configurations. The various configurations which can be done are such as changing the password for default user, the configuration settings are done according to the users need.
After the configuration settings are done, the python program is to be typed in the leaf pad. Leaf pad is created by file manager->right click->create->blank file->enter a file name.py- > click ok.
Next the program is saved. A web page is designed and PHP Script written in leaf pad also and saved as index.php. The first ZigBee configured to work as coordinator linked with Raspberry Pi, The second XBee configured to work as Endnode. The (op-amp) IC circuit connected to current sensor and the output of circuit connected to XBee shown in figure 2. Raspberry Pi is connected to the internet through the Router, and Router configured to forward port 80 to Raspberry Pi to work as web server. We accessed to main web page of power strip through Smart phone shown in figure 3. Using IP address. The various devices like Lights ON/OFF can be controlled shown in figure 4. 70 W and 40 W bulbs are plug in power strip separately. Directly power data appear in web page.

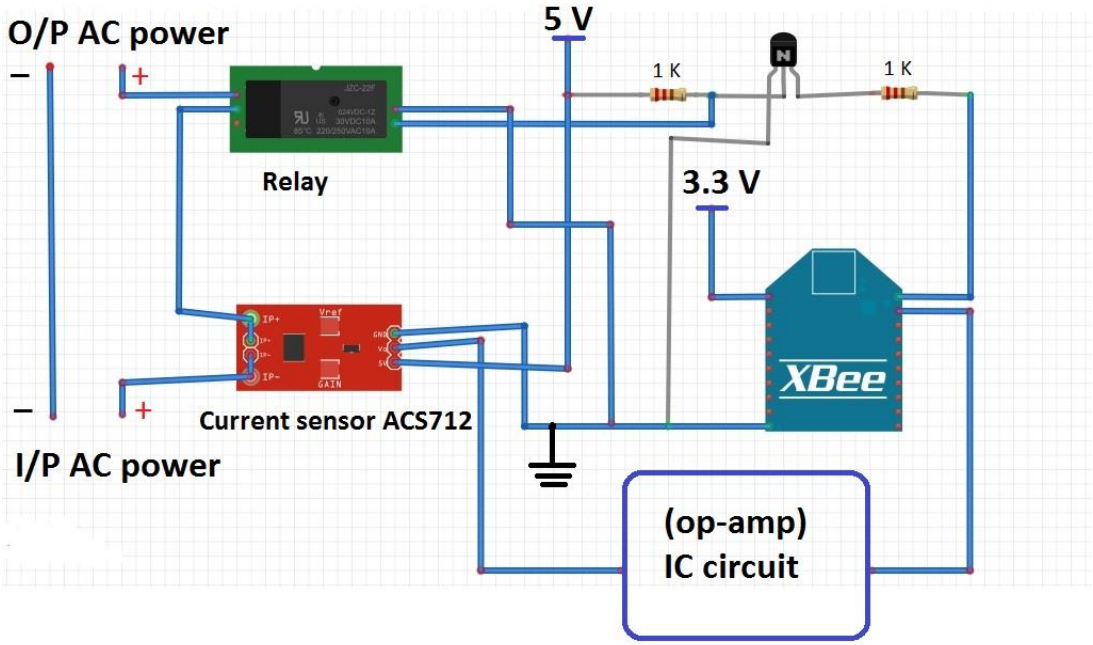

Figure 2: Circuit diagram

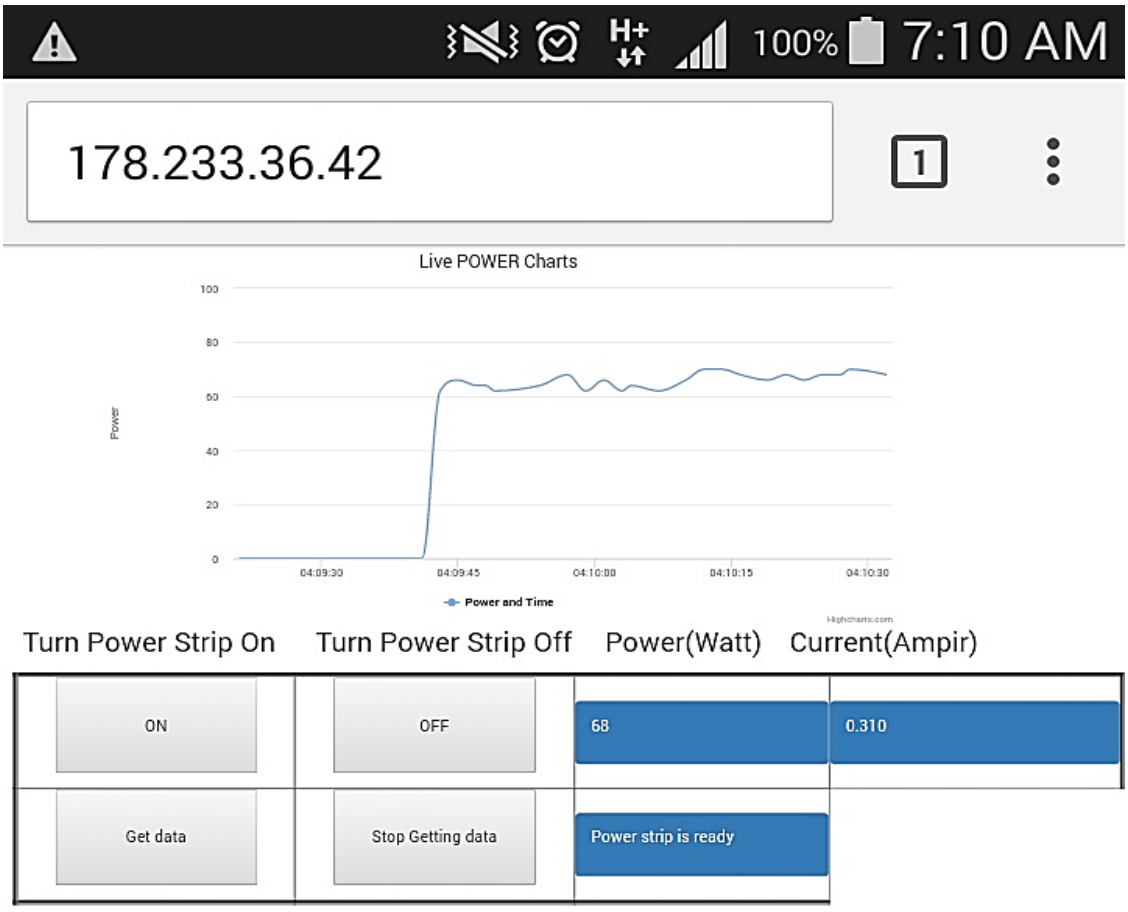

Figure 3: Power strip web-page

Figure 4: Controlling the bulb by using tablet

CONCLUSION AND FUTURE APPLICATIONS

In this paper, we have presented our development for wireless power strip to remote control and current sensing in order to manage home appliances. We developed the power strip along with a cost effective using minicomputer (raspberry pi) and ZigBee communication protocol. The raspberry Pi is configured to work as web-server and different Languages used to design a web-page as a platform for monitoring and controlling. The main advantage of our proposed work is to make the home owners able to manage home appliances remotely anywhere and anytime over the internet. It had been developed to be scalable to add more nodes and can add different sensors as required.
So that, a part of our future work is to develop the system to adapt with different places hospitals, hotels, banks, etc.

REFERENCES

Abo-Zahhad, M. A., & Ali, A. (2015). Design and implementation of building energy monitoring and management system based on wireless sensor networks. *In Computer Engineering & Systems (ICCES), 2015 Tenth International Conference on*, (pp. 230-233).
Chen, J. F., & Chen, T. (2008). A java development platform in mobile system for smart home. *In Future Generation Communication and Networking, 2008. FGCN'08. Second International Conference on*, (Vol. 2, pp. 226-229).

HAN, J., LEE, H., & PARK, K.-R. (2009). Remote-controllable and energy-saving room architecture based on ZigBee communication. *IEEE Transactions on Consumer Electronics, 55(1)*.

Lamine, H., & Abid, H. (2014). Remote control of a domestic equipment from an Android application based on Raspberry pi card. *In Sciences and Techniques of Automatic Control and Computer Engineering (STA), 2014 15th International Conference on*, (pp. 903-908).

LIEN, C.-H., BAI, Y.-W., & LIN, M.-B. (2007). Remote-controllable power outlet system for home power management. *IEEE Transactions on Consumer Electronics, 53(4)*.

Pavithra, D., & Balakrishnan, R. (2015). IoT based monitoring and control system for home automation. *Communication Technologies (GCCT), 2015 Global Conference on*, (pp. 169-173).

Withanage, C. A., & Otto, K. (2014). A comparison of the popular home automation technologies. *In Innovative Smart Grid Technologies-Asia (ISGT Asia), 2014 IEEE*, (pp. 600-605).

SIZE EFFECT ON PUNCHING SHEAR BEHAVIOR OF SLAB-COLUMN ASSEMBLY MADE FROM ENGINEERING CEMENTITIOUS COMPOSITE MATERIALS WITH POLYVINYL ALCOHOL FIBERS

Ali Kadhim H. ALHUSSAINAWE
Gaziantep University, Department of Civil Engineering, Gaziantep, TURKEY
engali77@yahoo.com

Farid H. ARNA'OT
Gaziantep University, Department of Civil Engineering, Gaziantep, TURKEY
farnaot@gmail.com

Ahmmad A. ABBASS
Gaziantep University, Department of Civil Engineering, Gaziantep, TURKEY
engaaa78@gmail.com

Mustafa OZAKCA
Gaziantep University, Department of Civil Engineering, Gaziantep, TURKEY
ozakca@gantep.edu.tr

ABSTRACT: Engineering Cementitious Composite (ECC) materials with PolyVinyl Alcohol (PVA) fibers are employed to investigate the effect of the ductile matrix on the behavior of flat plate-column connection. Totally four slabs are cast and tested, three of PVA-ECC slabs are compared to control slab of normal concrete. The thickness of the slabs used was variable (50, 60 and 80 mm) in order to investigate the effect of the size, and keeping the other size is constant (500 × 500 mm). All four slabs are reinforced with same conventional reinforcement ratio. The results showed that in the ductility of the slabs made from PVA-ECC are significantly enhanced compared with the normal concrete slab, this ductility improvement decrease with increasing the slab thickness, and more over the shear stress in the specific location is reducing with increasing the slab thickness.

INTRODUCTION

Flat plate-column assembly is one of most important connection members in structural system, especially when the height of the story is preferable. This connection is however governed by brittle punching shear failure. Many attempts and had been conducted to decrease the effect of the brittleness of the punching shear behavior, such as, using special shear reinforcement. Recently, the researchers seek to increases the ductility with keeping the same amount of the flexural reinforcements. However, the effect of slab thickness is still of the matrix aggravated the brittleness problem. Many researchers had been observed that increasing in the thickness of the slabs will rapidly decrease the shear stress

resistance (Bazant & Cao, Brickle & Dilger and Mutton & Schwartz) however, not all codes of practice are considered the size effect, such as ACI318 (ACI318-14). Some codes are considered this effect but with deferent forms. Eurocode 2 (EN1992-1-1) and DIN1045 (DIN1045-2) represent the size effect (ξ) as $\xi = 1+ 200/d$. Brickle and Dilger (Brickle & Dilger) observed that when using ACI318's equation, only 89 % of nominal shear resistance was reached for the slab of 300mm thickness, this percentage decrease to be 64 % for the slab of 500 mm (Guandalini et al).

Many researchers had been proposed different factor to capture the size effect on the punching shear strength. Broms (Broms) proposed his size effect factor based on assumption that the initiation of the cracks at the compression zone in the early hydration stage has an important role, his factor is produced in term of compression depth (xpu) as $\xi = (0.15/xpu)1/3$, which in turns proportional with rebar ratio, the cubic root in term of effective depth ($\xi = (500/d)1/3$) is proposed by Shehata (Shehata). Regan (Regan) shows that the fourth root is best introducing the size factor in term of effective depth $\xi = (1/d)1/4$.
In the current work, slabs of different thickness made from PVA-ECC are cast and tested in order to investigate the effect of the size, on the punching shear strength. Authors of the current work demonstrate that the effect of size importantly needs further researches.

EXPERIMENTAL PROGRAM

Slab Geometry and Materials

The experimental program included casting and tested four flat plates of square shape that most convenient to fabricate, the length of the sides are 500 × 500 mm. Three slabs coded as (V5, V6, and V8) of PVA-ECC matrix reinforced by steel reinforcement bars in addition to 2 % by volume PVA fibers, the properties of the physical of PVA fibers are summarized in Table 1. The three slabs are compared to control slab of normal reinforced concrete. The main parameter is the effect of slab thickness (h), where the three slabs thicknesses were 50, 60, and 80 mm, and the control specimen is of 50 mm thickness. The column stub size (c) is constant for all slab thickness that is of 55× 55 mm steel plate.

The flat plates are designed as its corresponding conventional reinforced concrete slab, which fail due to punching shear effect; therefore all tested slabs were reinforced by one layer of convenient flexural reinforcement by ϕ5.3 mm deformed bars, with 400 MPa yield strength. The ends of reinforcement bars are bent by 90 deg, one additional bar in each direction of the free ends are added. The concrete cover was 15 mm at all slabs. The reinforcement ratio ($\rho = 1.2$ %) was constant for all slabs, so there are different spacing bars, Figure 1. shows the slabs reinforcements details.

Table 1. Physical Properties of Polyvinyl Alcohol (PVA)

Density	l_f	D_f	l_f/D_f	Tensile strength	Elastic modulus
kg/m^3	mm	mm	mm/mm	MPa	GPa
1260	6	0.015	400	1600	34

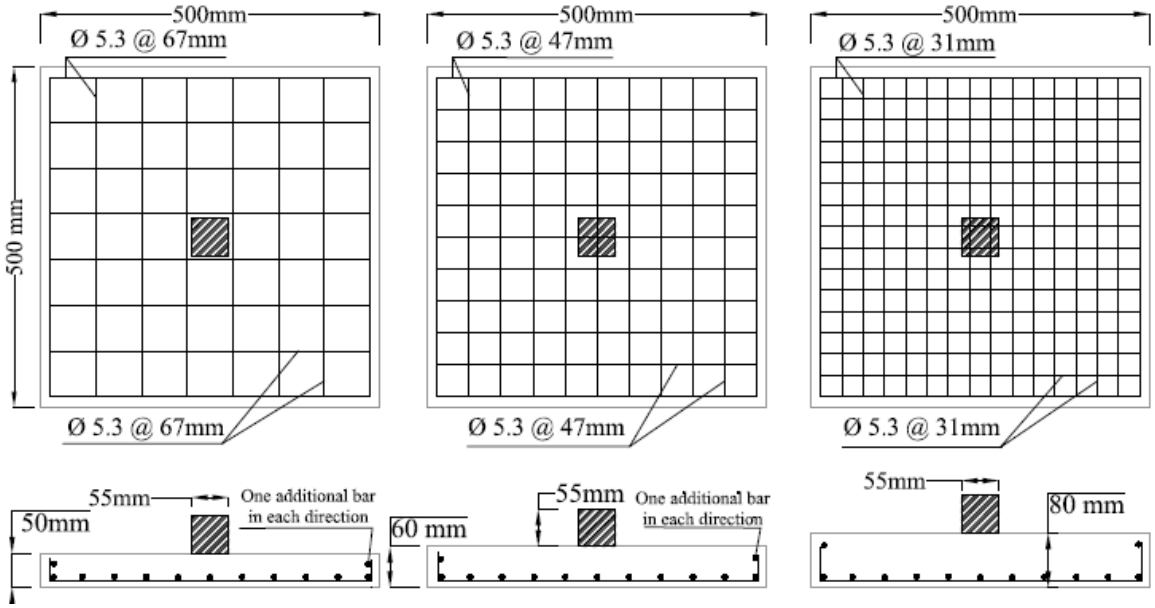

Figure1. Slab Geometry and Reinforcement Bars Details.

All slabs with PVA-ECC are cast in one batch, and the normal reinforced concrete slab is cast in a different batch. The materials used for the PVA-ECC slabs are summarized in Table 2. Portland cement of type CEM II/ A-LL 42.5 R for both ECC and normal concrete are used. The dense concrete is planned to use in the production of the normal concrete. The same mix proportion of Bazant and Cao (Bazant & Cao) recent work which is given in Table 2 are used for normal concrete where the fine aggregate content represents 63% of the total aggregate with 9.5 mm maximum size of aggregate, while the PVA-ECC does not include coarse aggregates. Therefore it can be regarded as fiber reinforced mortar. Dense nature of the two mixes is favourable to increase both concrete strengths (tensile and compressive), and increasing the interactions between the matrix and the fibers, and also to maximize the ductility by developing micro cracks.

The designed 28-days compressive strength (f 'c) of the standard cylinders (100 × 200 mm size) for the two mixes were 45 MPa, the actual compressive strength of the normal concrete and the PVA-ECC were 43.2 and 38.6 MPa, respectively. For the normal concrete mix, the dry materials are mixed for 10 minutes and then the water added with increasing the vertical mixer speed. For ECC, the dry binder materials (cement + fly ash) and the silica sand are mixed for three minutes at slow speed, after which the specified water is added with increasing the mixer speed to 30 minutes, in this stage the Superplasticizer is added for 2 minutes and

then the PVA fibers are interspersed by hand during the mixing. After mixing is complete the matrix is molded and externally consolidated for ECC, internally vibrated for normal concrete slabs, and rodded for standard cylinders. In order to overcome the errors, three standard cylinders were cast for each standard test, where the compressive and tensile strength are evaluated in this work. The slabs and the standard cylinders were kept for 24 hours in laboratory condition, and then cast specimens are mold and cured for 28 days in the water tank.

Table 2. Mix for the PVA-ECC and Normal Concrete

mix. code	Fiber	Water	Cement	Fly ash	Silica Fume	Sand	Crashing stone	Silica sand	Super plasticizer
	%	lt	Kg/m³	Kg/m³	Kg/m³	Kg/m³	Kg/m³	Kg/m³	Kg/m³
P	0	216	465	-	35	1170	680	-	6.6
V	2	352	551.4	662	-	-	-	441.12	7.33

Test Setup and Instrumentation

The test setup is followed the authors' recently work (Abo Altemen et al), where the slabs are supported on eight steel half balls, in order to represent the line of the contra flexure, the balls symmetrically distributed in a cycle of 400 mm diameter, the central angles were π / 4 as shown in Figure 2. The yield line analysis is based on Equation 1, that produced by (Guandalini et al.)

$$P_{flex} = \frac{4\, m_R}{r_q(\cos(\pi/8) + \sin(\pi/8)) - c} \times \frac{b^2 - (b \times c) - (c^2/4)}{b - c} \qquad \text{Equation 1}$$

Where, b, c, π, and r_q are depicted in Figure 2, the section moment capacity m_R are obtained as follows (Guandalini et al).

$$m_R = f_y \times \rho \times d^2 \times \left(1 - 0.5\rho \times \frac{f_y}{f'_c}\right) \qquad \text{Equation 2}$$

where d is the average effective depth of the section equal to $(d_1 + d_2)/2$, f'_c and f_y are the concrete compressive strength and bars' yield strength, respectively, and ρ is the reinforcement ratio taken as a sort of averaging as follows,

$$\rho = \frac{\rho_1 d_1^2 + \rho_2 d_2^2}{2d^2} \qquad \text{Equation 3}$$

In addition to the jack displacement of a test machine, the deflection at the centre of the slab is measured using Linear Variable Differential Transformers (LVDT) located at the centre of the bottom face. The monotonic increasing load is applied

through steel plate located at the centre of the slab; the load was applied in displacement control rate of 0.4 mm/min.

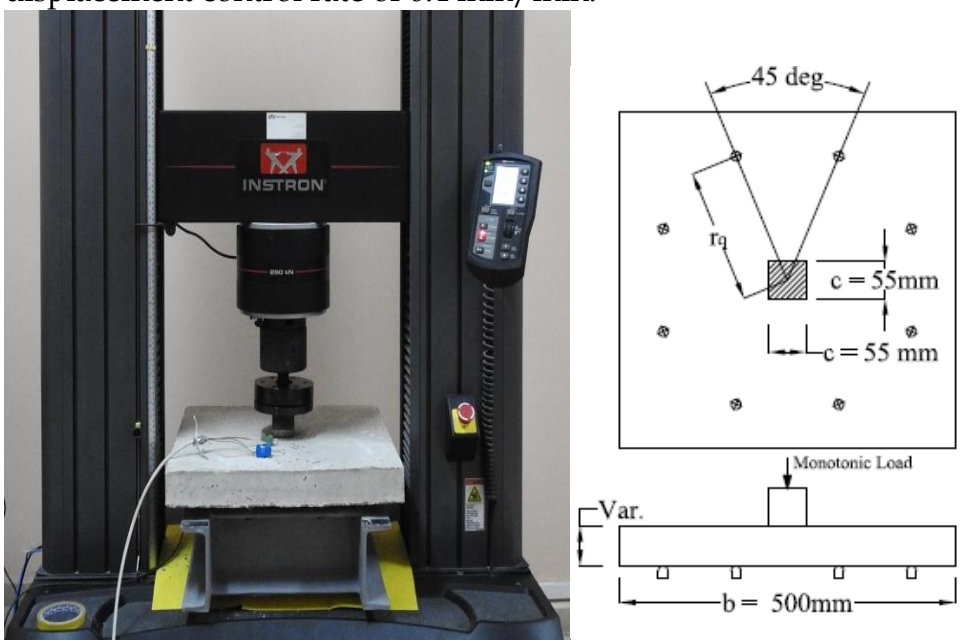

Figure 2. Test Setup and Supporting Details

EXPERIMENTAL RESULTS AND DISCUSSION

Punching Shear Strength

Table 3. summarized the test results. In spite of that f ´c of the normal concrete is higher than f ´c of the ECC, but the splitting strength (fsp) of the ECC were higher, it is shown that the correlation between the (fsp)to the square root of the f ´c was 0.59 which is close to correlation of the ACI318 [4] (0.556), while the correlation is increased 110 % for the ECC. This is not surprising because the ECC tends to form multi micro cracks between the first crack strain and the 1 % strain (Li, V.C.). The load required to initiate the cracks (Pcr) compared to ultimate load resistance (Pu) are increases with increasing the slab depth, the cracking load in ECC slabs are ranging between 7 and 14 % of the ultimate load, whereas the Pcr is initiated at 19 % of Pu for the specimen P (of normal concrete).

From the Table 3, it is shown that the slabs' strength increases with increasing the slab thickness, however, the flexural capacity are decreases (Figure 3a), that is lead to reduction in shear stress with increasing the slab thickness (see Figure 3b), this is agreed with Birkle and Dilger (Brikle & Dilger) finding. Comparing the ultimate strength with the nominal strength of the ACI318 (ACI318-14) and Eurocode 2 (EN1992-1-1) shows that these codes are conservative moreover; theses codes don't capture the effect of thickness on PVA-ECC. There are no differences between the two codes in prediction the punching shear for the V5, while the differences are increases with increasing the slab thickness. However, the proposed nominal strength by Birkle and Dilger (Brikle & Dilger) was not conservative and

overestimated the ultimate resistance (see Figure 3c), but the latter is best considered the size effect than the codes' equation.

Table 3. Summary of the Test Results

Spce. Code	Age	Density	d	f_{sp}	f'_c	$\frac{f_{sp}}{\sqrt{f'_c}}$	P_{cr}	δ_{cr}	P_u	δ_u	$\frac{P_{cr}}{P_u}$	P_{flex}	$\frac{P_u}{P_{flex}}$
	Day	Kg/m³	mm	MPa	MPa		kN	mm	kN	mm		mm	
P	45	2330	29.7	3.85	43.20	0.59	9.89	0.86	51.31	5.52	0.19	38.29	1.34
V5	49	1987	29.7	7.68	38.66	1.24	9.65	0.51	61.02	6.15	0.16	38.29	1.59
V6	48	1979	39.7	7.68	38.66	1.24	11.90	0.75	69.27	3.96	0.17	70.26	0.99
V8	40	2013	59.7	7.68	38.66	1.24	12.87	1.87	135.53	3.81	0.09	153.97	0.88

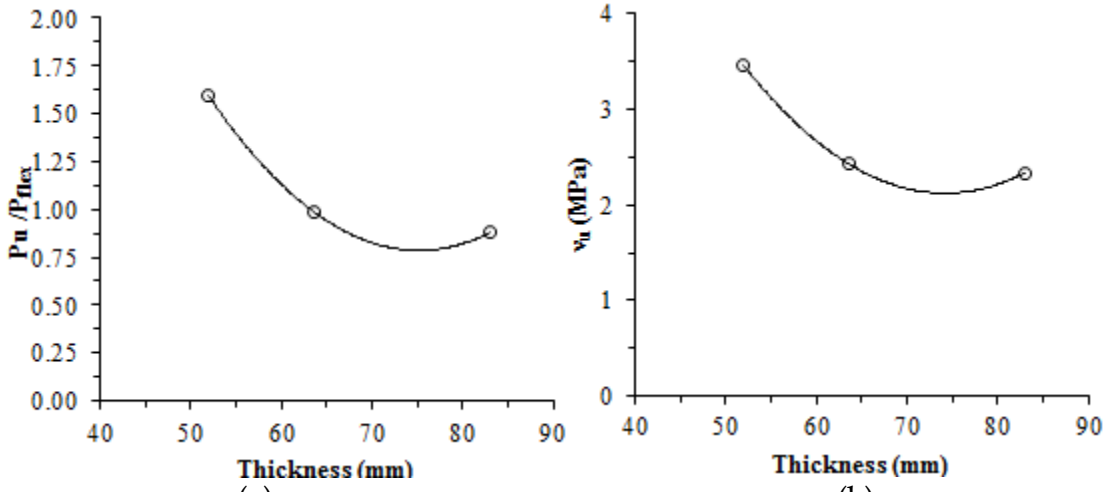

Figure 3. Effect Of Slab Thickness On (a) Flexural Capacity (b) Shear Stress (c) With Other Proposed Nominal Equations (ACI318-14, EN1992-1-1, Brikle & Dilger).

Load –Deflection Relationship

Figure 4. shows the deflection response under increasing monotonic loading, The loads are applied to the tested specimens up to failure, however, the curves show the response up to 50 % of the Pu, this is based on the authors experience, where the effect of tensile membrane action are included at this level, the deflections in Figure 4 are recorded from the LVDT placed at the center of slabs. It is shown that $\Delta P/\Delta\delta$ of the PVA-ECC slabs are more than the slab of the normal concrete, moreover, $\Delta P/\Delta\delta$ are decreases with decreasing the slab thickness. At the failure zone (beyond δu) It is showing that the load of the slabs of 60 and 80 mm (V6 and V8) are decreased sharply, this behavior also shows in specimen P (slab of normal concrete), whereas the slab V5 the load is gradually decreasing in the failure zone. Based on these premises, the ductility of the slabs is decreased significantly with increasing the slab thickness. Table 4 summarized the ductility of the tested slabs, the ductility refers to the efficiency of the materials to sustain the deformation before a collapse, the ductility quantified here in as a ratio of the deflection corresponding to 50 % of ultimate load to the deflection at first crack. From Table 4, it is clear that the ECC slabs show high ductility index than the slab of normal concrete, where the ductility index for V5 is more than that for P by 308 %, however, increasing the thickness of slab from 50 mm to 80 mm is reduced the ductility index by 25 %.

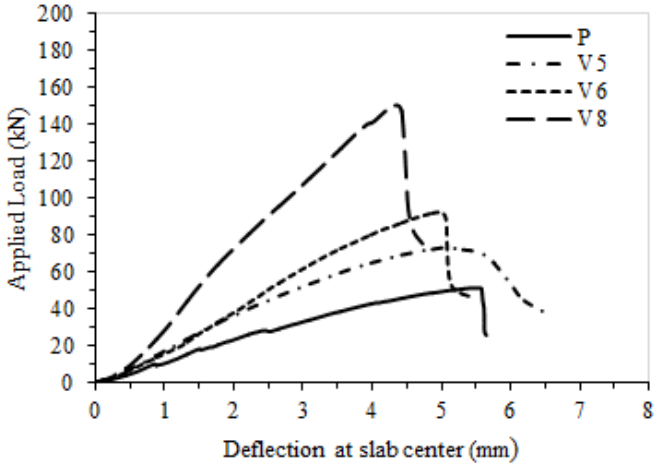

Figure 4. Load-Deflection Curves for ECC Reinforced Slabs

Table 4. Ductility And Failure Mode

Spec. Code	d mm	P_u kN	l_{cr}† mm	μ	Failure Type
P	29.7	51.31	2.5d	2.5	P+F
V5	29.7	61.02	2.7d	10.4	P+F
V6	39.7	69.27	1.9d	6.9	P
V8	59.7	135.53	1.4d	7.8	P

† l_{cr} is the distance from the column face to the punching shear crack in term of effective depth d

Cracks Pattern

The slabs designed to fail due to punching shear, the design applied to normal reinforced concrete in order to compare the effect of using high tensile and ductility materials. All slabs show the punching cone in deferent load levels. The important finding is that increasing the thickness is decreases the distance (lcr) from the column face to the punching circular crack. lcr is represented in term of d, where lcr is equal to 2.7 d in V5 this distance is reduced to 1.4 d in V8 with reduction of 48 % (see Table 4). That is means that the variation of the thicknesses is significantly affected the deformation.

Figure 5 shows the cracks patterns, where the failure of the ECC slabs are ranging between the uncompleted circle and completed circle, however, the slabs of 50 mm thickness of ECC and normal concrete shows radial cracks extended to edges of the slabs. Table 4 shows the type of failures. Moreover, it is recognised that the thicker slab shows more cracks than that thinner; this is because of the brittle behaviour of the thicker slab in addition to the congestion of the reinforcement bars.

CONCLUSIONS

Tests on slabs made from PVA-ECC materials, and with 50, 60, and 80 mm thickness, the control slab of normal concrete is designed due to in punching shear. The important conclusions driven from the current work can be summarized as follows,

Increasing the slab thickness was increased the ultimate punching shear strength, moreover, reducing a flexural capacity of the section and the shear stress at distance of d/2.

The total deformations are reduced with increasing the slab thickness, and the thicker slabs tend to fail due to punching shear.

The proposed codes equations [4] [5] of the nominal punching shear strength are significantly under estimated the tested slab, and not captured the effect of slab size.

Using PVA-ECC materials are significantly enhanced the ductility of the slabs compare to the normal concrete slabs.

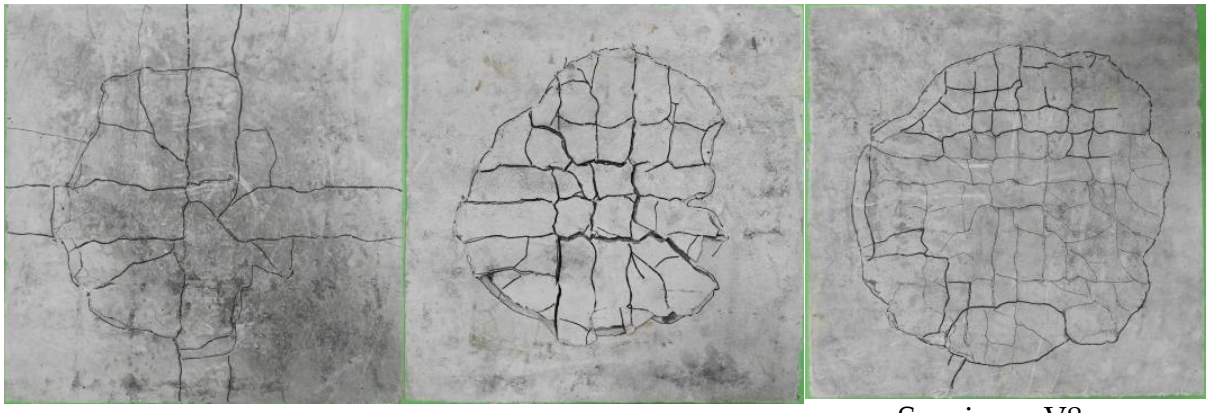

Specimen V5
Pu= 61.02 kN f'c = 38.66 MPa
d = 50 mm

Specimen V6
Pu= 69.27 kN f'c = 38.66 MPa
d = 60 mm

Specimen V8
Pu=135.53 kN f'c = 38.66 MPa
d = 80 mm

Specimen P
Pu= 51.31 kN f'c = 43.20 MPa
d = 50 mm

Figure 5. Cracks patterns of panels

REFERENCES

ACI318-14. (2014) Building Code Requirements for Structural Concrete (ACI 318M-14) and Commentary. *American Concrete Institute*, Farmington Hills, MI, ACI 318,-14.

Abo Altemen, A.A., Arna'ot, F. H., Abbass, Ahmmad. A.& OZAKCA ,M. (2017). Punching Shear Behavior of Small SFRC Flat Plate. Proceeding ICOCEE Cappadocia 2017:*2nd International Conference on Civil and Environmental Engineering*. Nevsehir, TURKEY, 891-901.

Bazant, Z. P. & Cao, Z. (1987). Size Effect in Punching Shear Failure of Slabs. *ACI Structural*, Title no. 84-S6, 44-53.

Brikle, G. & Dilger,W. H. (2008). Influence of Slab Thickness on Punching Shear Strength. *ACI Structural Journal*, 105(2), 180-188.

Broms, C. E. (2005). Concrete Flat Slabs and Footings Design Method for Punching and Detailing for Ductility. *Royal Institute of Technology,* Stockholm, Ph.D Thesis.
DIN1045-2. (2008). Concrete reinforced and pre-stressed concrete structures- Part 1: *Design and construction*, August 2008.

EN1992-1-1.(2004). Eurocode 2: Design of concrete structures - Part 1-1: *General rules and rules for buildings*. CEN, Brussels.

Guandalini, S., Burdet, O.L. & Muttoni, A. (2009). Punching Tests of Slabs with Low Reinforcement Ratios. *ACI Structural Journal*, 106(1), 87-95.

Li, V.C. (2007). Engineered Cementitious Composites (ECC) – Material, Structural, and Durability Performance. *In Concrete Construction Engineering Handbook*, New York: CRC Press,**.**

Mutton, A. & Schwartz, J. (1991). Behavior of Beams and Punching in Slabs without Shear Reinforcement. *IABSE Colloquium*, 62, 703-708.

Regan, P. E. (1981). Behavior of Reinforced Concrete Flat Slabs. *CIRIA Report 89 (Construction Industry Research and Information Association)*, Press London.

Shehata, I. (1990). Simplified Model For Estimating The Punching Resistance Of Reinforced Concrete Slabs. *Materials and Structures/ Materiaux et Constructions*, 23, 364-371.

EFFECT OF STEAM CURING BY SOLAR ENERGY ON THE MECHANICAL STRENGTH AND DURABILITY OF CONCRETES

Ben Khadda BEN AMMAR
Department of Civil Engineering, University of Biskra, Algeria
babkdeba_fr@yahoo.fr

Bouzidi MEZGHICHE
Department of Civil Engineering, University of Biskra, Algeria
bmezghiche@yahoo.fr

ABSTRACT: The influence of atmospheric steam curing by solar energy on the mechanical strength for precast concrete elements was investigated. An experimental program was carried out to study in parallel the effect of water/cement ratio (0.4, 0.5 and 0.6), the influence of cement type and the influence of curing methods (four methods of curing were used: water curing, air curing, steam curing at 29°C and steam curing at 45°C) on the compressive and flexural strength of samples concrete. Six similar formulations of workability are made from ordinary Portland cement (CEM I 42.5) and a compound cement (CEM II/B 42.5), three of each type are studied. The results obtained flow highlight the beneficial effect of a steam curing procedure to achieve high compressive and flexural strength, especially in the earlier ages of curing. However, after 28 days of steam curing, a strength reduction was observed in all samples.

Key words: concrete, mechanical strength, steam curing, solar energy, precast elements.

INTRODUCTION

Atmospheric steam curing is a heat treatment which has been used for many years to accelerate the strength development of precast concrete products. Because of the hydration rate of cement increases with the increase in temperature, the gain of strength can be speeded up by curing concrete in steam. When steam is generated in atmospheric pressure, the temperature is below 100 °C; the process can be regarded as a special case of moist curing in which the vapour-saturated atmospheres ensures a supply of water (Hanson J.A.1963 and Neville A.M.1981).
It is confirmed that the steam curing at low pressure could improve the quality of high performance concrete incorporating mineral admixtures, comparing with standard curing (Maltais Y et al. 1997).

The curing temperature will be a compromise between rate of strength gain and ultimate strength, because of the higher, the curing temperature, the lower and the ultimate strength (Mindess et al. 1981).

The primary factors determining the behavior of cements subjected to heat treatment are fineness and composition of cements, the type and amount of additives used in blended cements and curing cycle parameters. For compressive strength development of concrete, duration of steam curing is also an important parameter as well as temperature (Oztekin E. 1984).

Erdem et al. (2003) concluded that in the delay in the commencement of steam curing operation by a period equal to the initial setting time of cement, higher strengths were obtained when the delay period was equal to the setting time. However, it is clear that the effect of the humidity during curing is a major consideration that cannot be ignored. Steam curing continues until the minimum is reached strength deemed essential to the performance of the element after demolding (Vénuat M. 1989), this minimum would be difficult to determine a priori because it depends on the shape more or less massive parts, and depends on the nature of the stresses to which they submitted after release. To fix ideas, we may admit that in the absence of any external load, the minimum strength to compressive should be located around 50 to 60% of the required strength (at 28 days under natural conditions) is 10 MPa (ACI 517.2R-87. 1992), which can transport and store the parts in concrete rooms for a natural hardening to ambient air in the realization of business without breaking.

The required objective is to evaluate through experiments the influence of atmospheric steam curing on the mechanical strength of concrete.

Experimental Program

In this section we present the materials used, formulation of concrete and the preparation of specimens.

Materials

Cement

The cement that was used is composed Portland cement CEM II/B 42.5 (Biskra - Algeria). Fineness = 3300 cm^2/g, apparent density = 1215 kg/m^3 and specific density = 3150 kg/m^3.

Water

The water is drinking water and having a temperature of 20 ± 1°C. Its quality conforms to the requirements of standard NFP 18-404.

Sand

The sand used is from the region of Biskra (Algeria). The grading curve of sand is given in fig.1. Apparent density = 1630 kg/m^3. Specific density = 2650 kg/m^3, Fineness modulus = 2.82

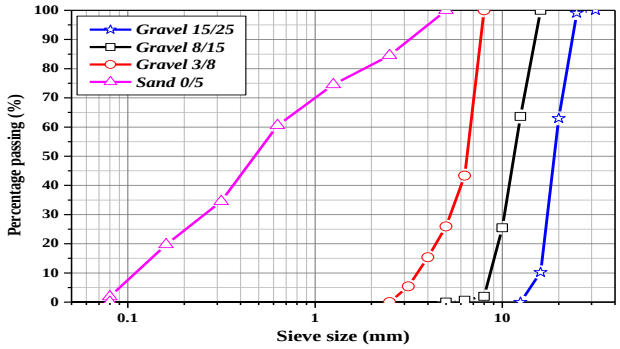

Figure 1. Grading Curve Of Sand And Crushed Stone

Crushed stone

We used crushed stone (CS) fraction 3/8, 8/15 and 15/25 mm of the region Batna in Algeria. The grading curve of crushed stone is given in figure 1, Apparent density = 1340 kg/m^3, Specific density = 2610 kg/m^3.

Study of the temperature in the steam curing chamber and at ambient air

Our study is first to raise the temperatures in the open air using a thermometer and within the confines of conservation (Figure 2) by other thermometers hourly and daily same time of 07 h to 21 h for 12 months of the year, the average of these monthly records are illustrated in figure 3.

Figure 2. Steam Curing Chamber

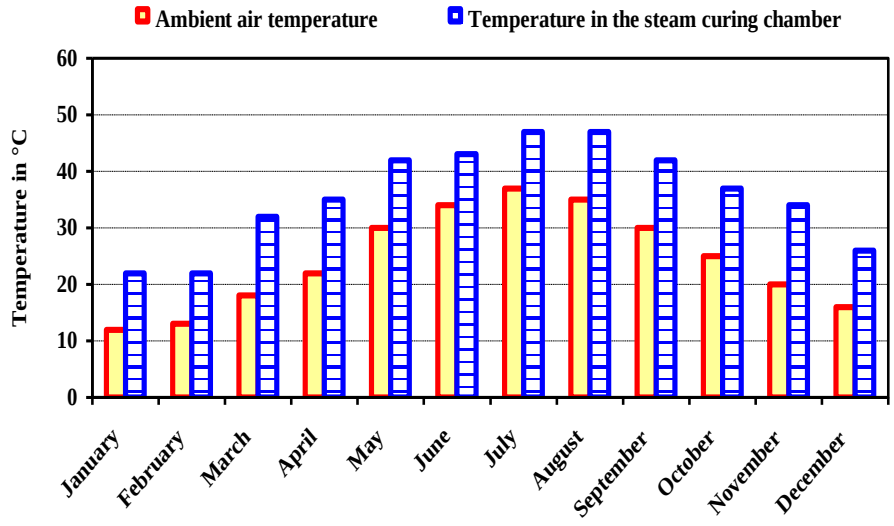

Figure 3. Monthly Exchange In Outdoor Temperatures And The Steam Curing Chamber

Formulation of concrete

Optimizing the formulation of concrete based on several criteria that are often a compromise between them: consistency, strength, durability and economy. Before the multiplicity of methods used to determine the composition of concrete was used that gives accurate results and seems to be the least known. This is the method of B. Scramtaiv. Whose consistency is such that its cone slump of 7 cm. In all tests the w/c = 0.4, A = 0.6, D_{max} = 25 mm and S/CS = 0.33. The composition of concrete is reported in table 1.

Table 1. Composition of Concrete (kg/m^3)

Cement	Sand	Crushed stone (7/15)	Crushed stone (15/25)	Water
512	407	432	802	205

From the graphs of the temperature variation with time of 12 months, we can say that for six months from April to September, the average temperature coefficient (K_1 = 1.70), and October to March, the average temperature coefficient is: (K_2 = 1.40). With: T° is the temperature in °c and K: the average temperature coefficient (K = 1.55). Based on the findings deduced from the variation curves of temperature versus time inside the chamber, we select the six months which corresponds to the seasons: spring and summer as shown in Table 2.

Table 2. Steaming Cycles And Maximum Temperatures In The Room (Spring-Summer)

Month	Apr	May	Jun	Jul	Aug	Sept
Cycles	3×8×3	3×8×3	3×8×3	3×9×3	3×9×3	3×8×3
Max. T°	38	43	44	46	48	43

We opt for steam curing cycle 1: (3×8×3) with a maximum temperature bearing 45 °c. We do the same for the other six (06) months representing the fall and winter and the pattern of the cycle.

Table 3. Steaming Cycles And Maximum Temperatures In The Room (Autumn - Winter)

Month	Oct	Nov	Dec	Jan	Feb	Mar
Cycles	3×8×3	3×7×3	3×7×3	3×7×3	3×7×3	3×8×3
Max. T°	34	32	30	28	23	34

We opt for steam curing cycle$_2$: (3×7×3) with a maximum temperature bearing 29°c.

Preparation of specimens

The strength is expressed by the power of concrete to resist destruction under the action of stresses due to different compressive loads and flexural.
Specimens of cubic (100×100×100 mm) were produced to determine the compressive strength, other form of prismatic (100×100×400 mm) to determine the flexural strength.
The concretes studied: a control concrete stored in water at an ambient temperature of 20 ± 1°c, concrete cured outdoors without irrigation, and concretes subjected to two cycles of steam curing.
The steam curing cycle must include four phases: delay period; temperature rises; maximum temperature and cooling.
After mixing the concrete, the specimens are preserved in plastic to prevent evaporation of water from the concrete, after demolding, the specimens are introduced into the steam curing chamber by solar energy with the rise of the temperature in the chamber, the thermometer was placed outside of the chamber can adjust the temperature level selected at 45°c in the chamber for the warm period of the year.
(6 months from October to March) and 29°c for the cold period (6 months from April to September), for durations of steam curing 1, 2, 3 and 7 days hardening in open air without spraying of 3 and 7 days.

RESULTS AND DISCUSSIONS

Consistency
It is important to know the properties of concrete in fresh state before setting and hardening. Among these properties, consistency can be defined as the ease of implementation of concrete.
The slump test to Abrams cone NF P 18-451 is currently in use worldwide. Depending slump obtained, class consistency of different concrete is plastic (slump varies from 6 to 8 cm).

Compressive and flexural strength

The strengths are estimated at 1, 2, 3 and 7 days of steam curing, 28 days in wet and dry.

The results of compressive and flexural strength of concrete in water, the open air and concretes having undergone a steam curing are given in figure 4 (a, b, c and d), 5 and 6 respectively.

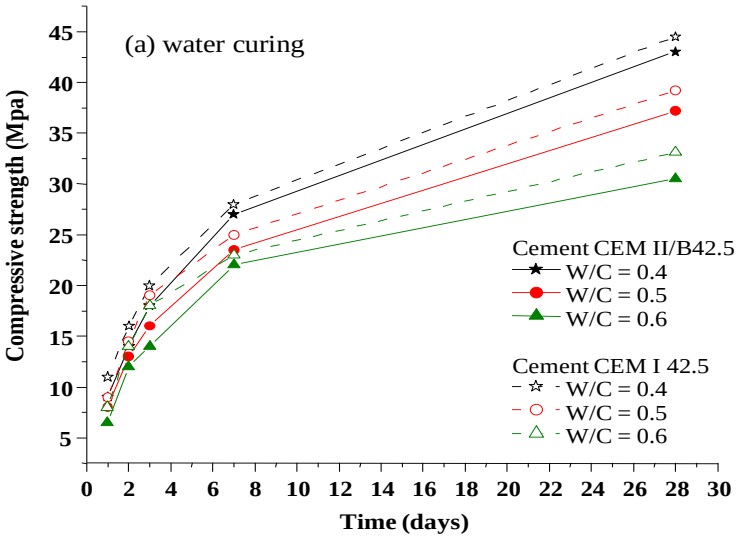

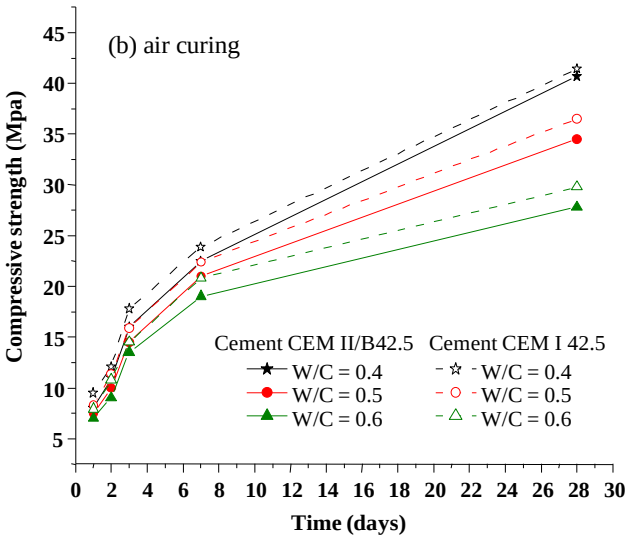

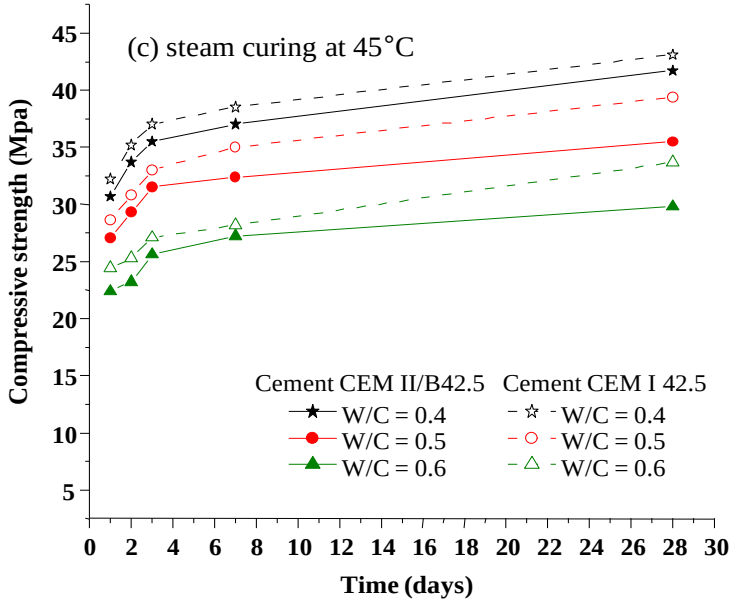
(c) steam curing at 45°C
Compressive strength (Mpa)
Time (days)
Cement CEM II/B42.5
W/C = 0.4
W/C = 0.5
W/C = 0.6
Cement CEM I 42.5
W/C = 0.4
W/C = 0.5
W/C = 0.6

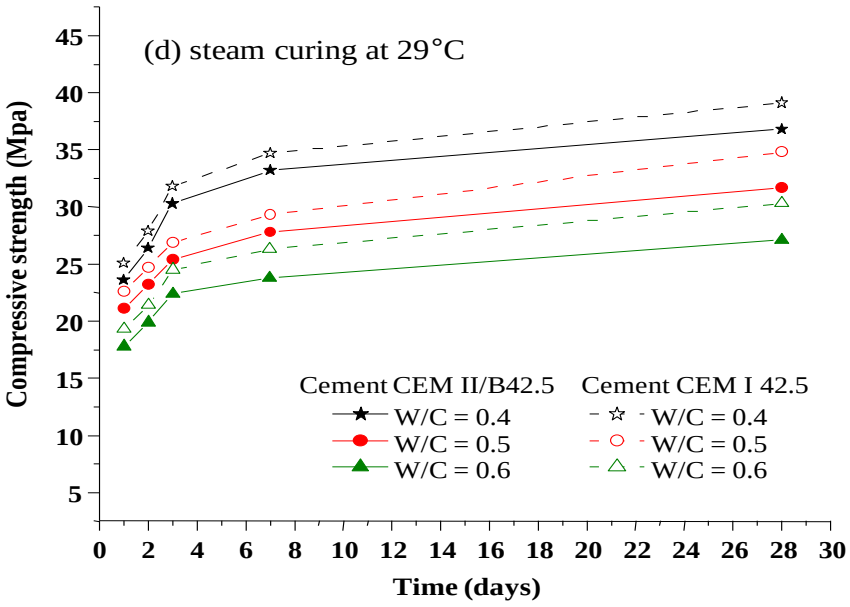
(d) steam curing at 29°C
Compressive strength (Mpa)
Time (days)
Cement CEM II/B42.5
W/C = 0.4
W/C = 0.5
W/C = 0.6
Cement CEM I 42.5
W/C = 0.4
W/C = 0.5
W/C = 0.6

Figure 4. Effects Of Curing Methods, Cement Type And W/C Ratio On The Compressive Strength Development Of Samples

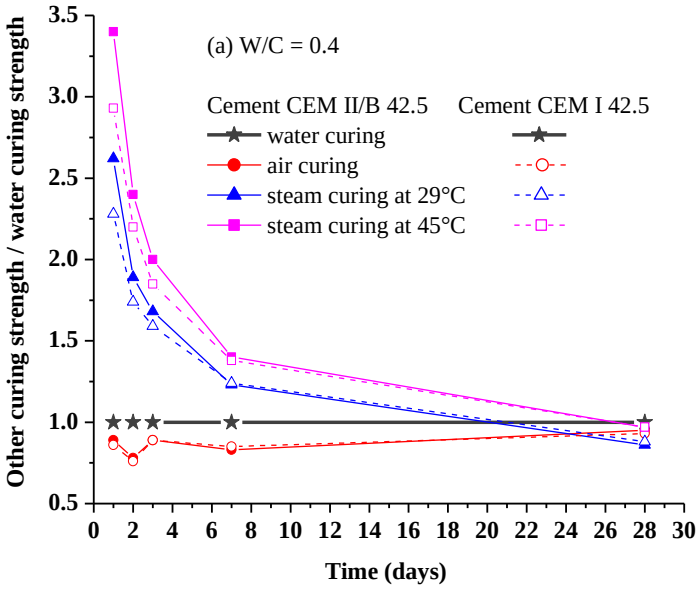

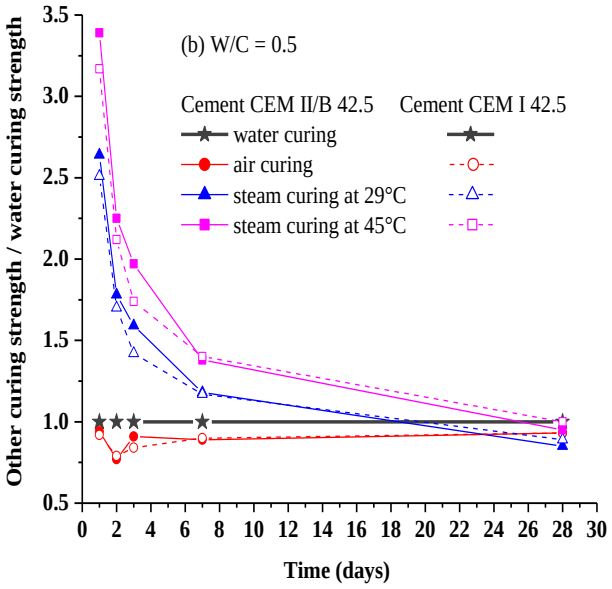

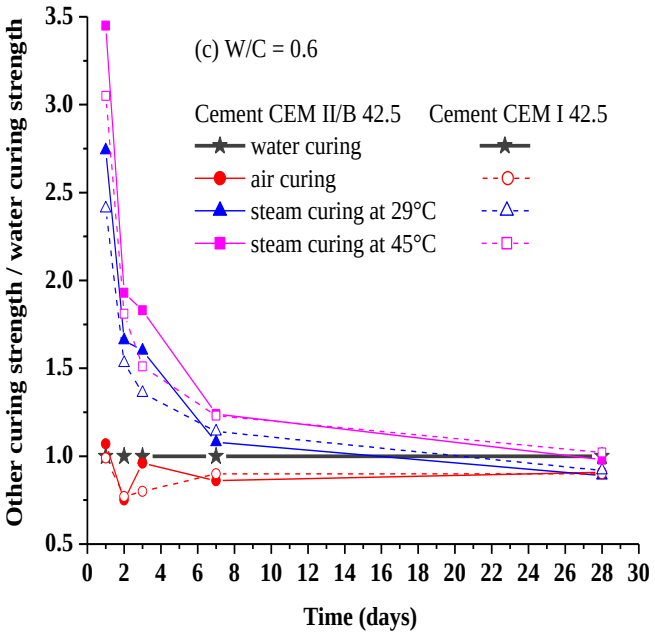

Figure 5. Effects of Curing Methods, Cement Type And W/C Ratio On The Compressive Strength Ratio Of Samples

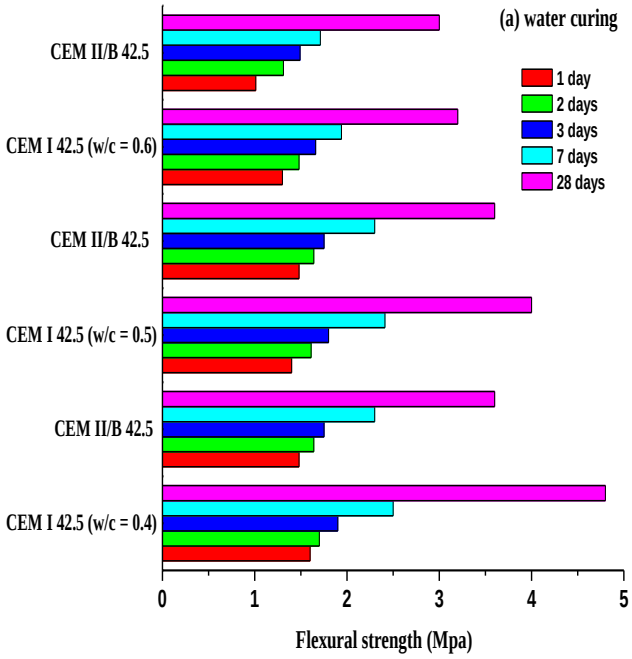

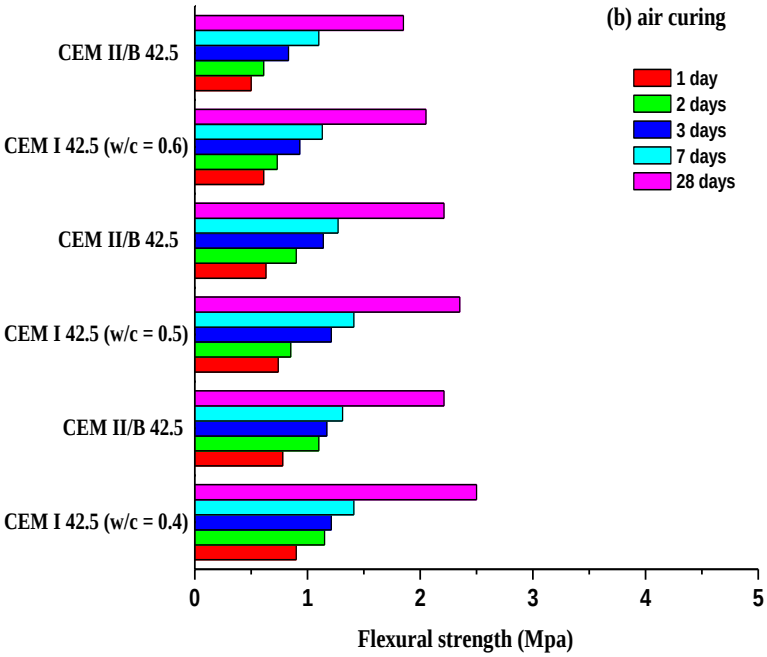
(b) air curing
1 day
2 days
3 days
7 days
28 days
CEM II/B 42.5
CEM I 42.5 (w/c = 0.6)
CEM II/B 42.5
CEM I 42.5 (w/c = 0.5)
CEM II/B 42.5
CEM I 42.5 (w/c = 0.4)
0
1
2
3
4
5
Flexural strength (Mpa)

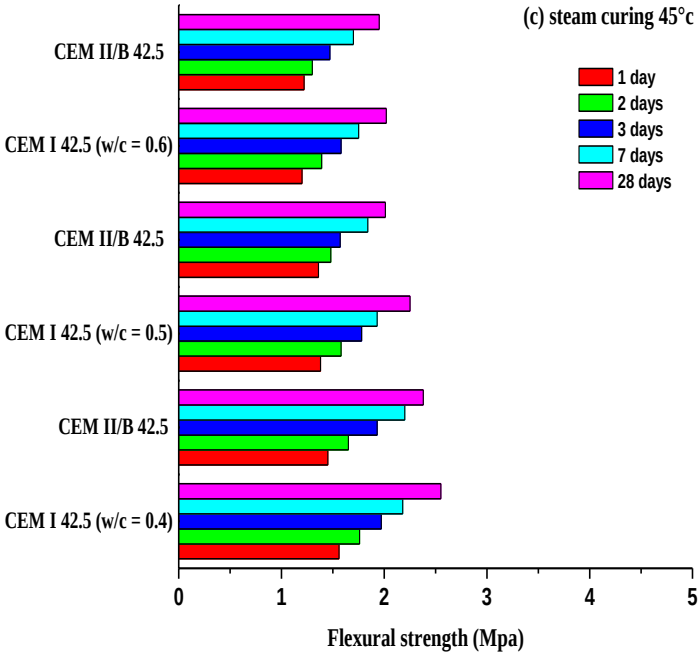
(c) steam curing 45°c
1 day
2 days
3 days
7 days
28 days
CEM II/B 42.5
CEM I 42.5 (w/c = 0.6)
CEM II/B 42.5
CEM I 42.5 (w/c = 0.5)
CEM II/B 42.5
CEM I 42.5 (w/c = 0.4)
0
1
2
3
4
5
Flexural strength (Mpa)

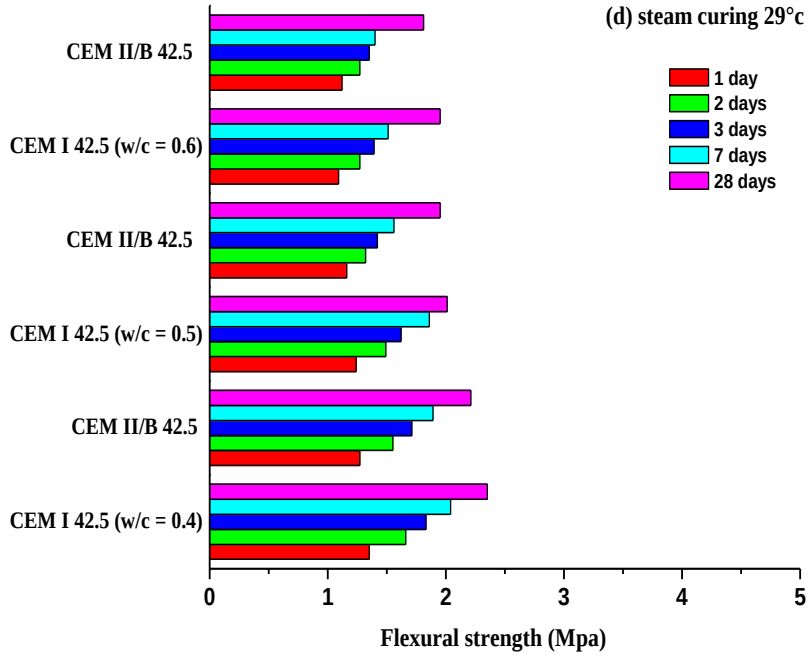

Figure 6. Effects Of Curing Methods, Cement Type And W/C Ratio On The Flexural Strength Development Of Samples

Extension of hardening of concrete in the open air

One day of steam curing at 45°c and hardening of 3 and 7 days

The strengths estimated from (1d steam curing and air 3d) and (1d steam curing and air 7d) for steam curing at 45°c are shown in table 4.

Table 4. Compressive And Flexural Strength Of Concrete (1d Steam Curing At 45°C + Air 3 And 7d)

Strength (MPa)	1d steam curing + air 3d	(%) harden	1d steam curing + air 7d	(%) harden
Compressive	40	99	43	105
Flexural	1.80	82	2.00	90

The period (spring - summer) at 45°c, the months of April-September results show that treatment with steam curing in the chamber ensures a rapid increase in compressive strength for: 1, 2, 3 and 7 d of steam curing at 45°c, are: 30.7, 33.7, 35.5 and 37.0 MPa, which are: 75, 83, 87 and 91% of the strength of hardened concrete even under natural conditions to 28 days respectively.

- Compressive strength of one day steam curing at 45°c (08 h of oven) and in air 3 and 7 d under natural conditions, which are: 40.3 and 43 MPa, are: 99 and 105% of

the strength of the hardened concrete even under ambient conditions at 28 days respectively.
- An increase in compressive strength and flexural strength versus time, which ensures demolding of the molds only 3 days in air.

One day of steam curing at 29°c and hardening of 3 and 7 days

The strengths estimated after (1d of steam curing and air of 3d) and (1d of steam curing and air 7 d) for steam curing at 29°c are shown in Table 5.

Table 5. Compressive And Flexural Strength Of Concrete (1d Of Steam Curing At 29°C + Air 3 And 7d)

Strength (MPa)	1d steam curing + air 3d	(%) harden	1 d steam curing + air 7d	(%) harden
Compressive	39.30	96.50	41	100
Flexural	1.43	64.70	1.62	73.30

The period (autumn - winter) at 29°c, for the months of October to March:
- One day of steam curing at 29°c: 23.6 MPa, which shows: 58% of the strength of hardened concrete even under natural conditions to 28 days.
- One day steam curing concrete at 29°c (08 h of steam curing) and in air 3 d under natural conditions, which presents: 39.3 MPa, or 96.5% of the strength of hardened concrete even under natural conditions to 28 days.
- One day steam curing concrete at 29°c and 7 days of hardening under natural conditions, which presents: 41.0 MPa, 100% of the strength of hardened concrete even under natural conditions to 28 days.
- An increase in compressive and flexural strength as a function of time, which ensures demolding of the molds only in 3 days in air.

Mass loss in the steam curing chamber at 45°c and 29°c

The quantification of the wastewater between the demoulding and the sample removal in the stoving chamber was carried out using a balance with a capacity of 10 kg and an accuracy of 0.01 g used for the determination of The mass of the specimens before and after the two cycles of hardening and curing in ambient air.
The results presented in Tables 6 and 7 indicate that the mass losses during stoving at 45 °C and 29 °C. between the demoulding and the test time for different ages of 3 and 7 of curing caused by the creation of very fine cracks By the expansion of the air bubbles in the cement and the evaporation of the water of the capillaries.

Table 6. Mass Loss In (gr) Of The Cubes And Prisms At 45°C

Specimens	air 28 d	Steam curing			
		1d	2d	3d	7d
Cubes	35	24	46	68	149
Prisms	110	90	130	185	240

Specimens	1d steam curing + air 3d	1d steam curing + air 7d
Cubes	30	45
Prisms	102	120

Table 7. Mass Loss In (gr) Of The Cubes And Prisms At 29°C

Specimens	air 28 d	Steam curing			
		1d	2d	3d	7d
Cubes	35	20	40	60	128
Prisms	110	80	120	175	220

Specimens	1d steam curing + air 3d	1d steam curing + air 7d
Cubes	27	40
Prisms	93	111

CONCLUSION

Add conclusions here. Add conclusions here. Add conclusions here. Add conclusions here. Add conclusions - The technique of steam curing is an effective technique for portlands cements for accelerated hardening of concrete.

- The demolding is assured after all steam curing at 45 or 29°c, since we met exceeds the minimum strength to compressive which is approximately 10 MPa after one day of steam curing, which ensures high productivity molds.
- We reached the 28 days strength after one day and 3 days of hardening in open air, for 2 types of steam curing, which has a gain of time and shorter manufacturing lead times.
- The plastic concrete works to heat treatment, for a temperature of 45°c in steam with 8 hours of heat treatment with a pre made, the strength reach 75% of the control concrete strength of 28 days of normal hardening, also the fall of mechanical strength at the age of 28 days of a concrete treated compared to concrete o f control is around 10%.
- This hardening technique in Algeria which is rich in solar energy and the use of this renewable energy in the heat treatment of concrete parts in areas with high radiation concentration and long periods, which reduces the cost of Concrete parts, resulting in a remarkable economy for production companies, as well as productivity changes for the concrete industry.

REFERENCES

Hanson J.A. (1963). Optimum steam curing procedure in precasting plants. American Concrete Institute. Proc. 1963;60(1):75-100.
Neville A.M. (1981). Properties of Concrete. Pitman Publishing Limited, London 1981. 544.
Maltais Y, Marchand J. (1997). Influence of curing temperature on cement hydration and mechanical strength development of fly ash mortars. Cement and Concrete Research 1997;27(7):1009-1020.
Mindess S, Young J.F. Concrete. Prentice-Hall, Inc., Englewood Cliffs, NJ. 1981.
Oztekin E. (1984). Determination of heat treatment cycle for cements. Turkish cement manufacturers. Association Cem. Bull. 1984;206(3):24-26.
ACI 517.2R-87 revised. (1992). Accelerated curing of concrete at atmospheric pressure-state of the art. American Concrete Institute, Farmington Hills Michigan. 1992. 17p.
Erdem T.K, Turanli L, Erdogan T.Y. (2003). Setting time: An important criterion to determine the length of the delay period before steam curing of concrete. Cement and Concrete Research 2003;33(5):741-745.
Vénuat M. (1989). The practice of cements mortars and concretes. 2nd edition. 1989. Volume 1:215-217.

ANALYSIS OF THERMAL TRANSPORT THROUGH A FLAT-PLATE SOLAR COLLECTOR INTEGRATED WITH METAL-FOAM BLOCKS

Ahmed ALBOJAMAL
University of California-Riverside
aalbojamal@engr.ucr.edu

Arman HAGHIGHI*
University of California-Riverside
ahaghighi@engr.ucr.edu

Hudhaifa HAMZAH
University of Mosul
hudhaifahamzah@gmail.com

ABSTRACT: Forced convective heat transfer in a solar water collector channel with three metal-foam blocks attached on the inside wall, is studied numerically. Darcy equation with the Brinkman and Forchheimer terms is used to analyze the flow in the porous section; and Local thermal equilibrium (LTE) is considered between the working fluid and the porous region. The fluid flow in the channel and the thermal behavior of the system are analyzed considering various parameters such as Darcy number, thermal conductivity ratio, porosity and Reynolds number. The results prevail that the generated recirculation zones between blocks will significantly improve the heat transfer rate from the heated surface; and metallic porous material can perform as effective heat exchangers in thermal applications such as electronic cooling and solar heat collectors.

Keywords: solar collector, metal foam, electronic cooling.

Nomenclature

A	aspect ratio, $A = H / H_{\mathrm{m}}$
C	inertia coefficient
c_p	specific heat $[J / kg \cdot K]$
Da	Darcy number
D_h	hydraulic diameter $[m]$
d_f	fiber diameter $[m]$
d_p	mean pore diameter $[m]$
F	Forchheimer coefficient
G	shape function
H	channel height $[m]$
h	local heat transfer coefficient $[W / m^2 K]$
K	permeability of the porous blocks $[m^2]$
T	temperature $[K]$
U	dimensionless axial velocity
u	axial velocity $[m / s]$
V	dimensionless transverse velocity
v	transverse velocity $[m / s]$
W	width $[m]$
X	dimensionless axial coordinate
x	axial coordinate $[m]$
Y	dimensionless transverse coordinate
y	transverse coordinate $[m]$

Greek symbols

k	fluid thermal conductivity $[W/mK]$
L	total length $[m]$
L_h	length of absorber plate under solar energy $[m]$
Nu	Nusselt number
P	dimensionless pressure
p	pressure $[N/m^2]$
Pr	Prandtl number
q''	solar heat flux $[W/m^2]$
R_c	thermal conductivity ratio
Re	Reynolds number
R_x	length ratio, $R_x = W_m/(W_m + S_m)$
R_y	height ratio, $R_y = H_m/H$
S	spacing $[m]$
ε	porosity
μ	dynamic viscosity $[Pa \cdot s]$
θ	dimensionless temperature
ε	porosity
ρ	density $[kg/m^3]$

Subscripts

e	outlet conditions
eff	effective
f	fluid
m	metal foam
o	inlet conditions
s	solid

* Corresponding author (Address all correspondence to: ahaghighi@email.ucr.edu)

INTRODUCTION

Thermal efficiency enhancement of heat exchanger has received significant attention by the researchers in order to meet the increasing demand to design and implement compact heat exchangers. Different techniques are utilized by the researchers presented in (Albojamal and Vafai, 2017; Wang and Chen, 2002; Chabane, 2014 and Lee and Vafai, 1999) for heat transfer enhancement. Some of them increase the overall thermal conductivity of the working fluid by dispersing small colloidal solid particles, 1-100 nm in diameter. While others worked on altering the surface geometry by using special channel wall shapes such as wavy or corrugated walls.

Direct solar radiation is one of the promising sources of renewable energy. Solar thermal collectors are a special type of heat exchangers that absorb the incoming solar radiation energy, and transfer it to the internal transport medium (Kalogirou, 2004). Flat-plate collectors are the most common type used in residential structures, space heating, and commercial or industrial applications where the demand for hot water has a large impact on energy costs (Kudish, 2002). There is a lot of effort focused on optimizing the flat-plate solar collector by means of reducing their size and increasing the fluid temperature at the outlet. With this goal, various different techniques has been introduced (Bashria et al., 2007; Chabane, 2014; Reddy and Satyanarayana, 2008). Despite the attractive thermal performance of these techniques, heat transfer in flat plate solar collectors still needs further development to reach higher heat transfer rates between heated surface and the fluid.

Metallic porous material has emerged over the past decade as a promising new technology for a wide range of applications, such as in compact heat sinks in electronic devices, chemical reformers, combustors and solar thermal collectors. This is due to the attractive thermo-mechanical features of metal-foams including high solid thermal conductivity, lightweight with high strength and rigidity, enhanced flow mixing capabilities of porous matrix and large surface area per unit volume (Lu et al., 1998; Banhart, 2001 and Zhao, 2012). Numerous studies have been carried out on forced convection with steady state flow through a channel partially or fully filled with a metal foam (Qu et al., 2012 and Lu et al., 2017). Angirasa (2002) presented a numerical study for heat transfer in a channel completely filled with rigid metallic materials with high porosity. Lu et al. (2006) analytically investigated the open-cell metal foam fully filled heat exchanger pipes. Their results confirmed that the use of metal-foam can dramatically enhance the heat transfer, but at the expense of a significant increase in the pressure drop. They showed that the pressure loss is three to four times higher than that of an empty channel. This situation impairs the application of metal foams for most engineering cases requiring low pressure drop. Also, for fully filled channel LTNE model is more accurate and should be used for the flow analysis according to Lee and Vafai (1999). While for partially filled duct, due to the relatively low velocity in the foam region, the temperature difference between solid and fluid phases is minimal and the LTE model may be employed (Xu et al., 2015).
Present study aims to numerically investigate the characteristics of fluid flow and heat transfer through a parallel flat-plate channel solar water collector with multiple metal-foam blocks mounted on the inside wall and by considering Local Thermal Equilibrium (LTE) in the solid-fluid interface. The essential heat and flow interaction between the metal-foam porous block and the working fluid, as well as the methodology of improving the rate of heat transfer near the heated surface and reduced the pressure drop are analyzed and discussed in this work. Our results were compared and validated with the numerical work of (Chikh et al. 1998).

MATHEMATICAL FORMULATION

The schematic for flat-plate solar collector for forced convection water flow is shown in figure 1 for current study. The water flow through a horizontal parallel-plate channel with three separate metal-foam porous blocks with height H_m and width W_m. The channel height is H and the total length is L. Constant heat flux q'' is imposed along the length of the absorber plate of length L_h. The remaining walls are insulated. The height (R_y) and length (R_x) ratios of the channel are set equal to 0.5 and 0.25 respectively. While the block width (W_m) and the spacing between them (S_m) set equal to each other. Furthermore, the fluid enters the channel with uniform inlet temperature T_o and parabolic fully developed velocity profile. A two-dimensional, laminar, incompressible and steady flow with constant thermophysical properties for both the fluid and metal-foam are considered. The buoyancy and radiation effects are neglected. Also, the porous

metals are considered as homogenous and isotropic. The area after the last block is chosen to be long enough to ensure fully developed conditions at the channel exit.

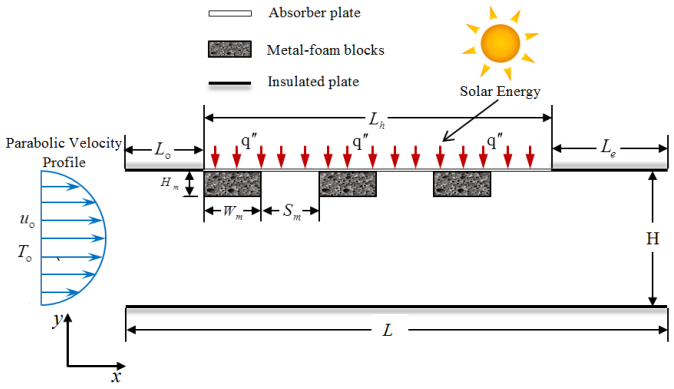

Figure 1. Configuration Under Current Study.

The momentum equations includes both Brinkman and Forchheimer terms to incorporate the viscous and inertial effects in the porous matrix, while Navier–Stokes is the governing equation in the fluid domain. For simplification, the angle brackets representing volume-averaged variables are dropped in equation pertaining to the porous domain, for example u in the porous region is equivalent toáuñ. Continuity in the fluid region:

$$\frac{\partial u}{\partial x}+\frac{\partial v}{\partial y}=0 \qquad (1)$$

Continuity in the porous region:

$$\frac{\partial u}{\partial x}+\frac{\partial v}{\partial y}=0 \qquad (2)$$

Momentum equation in the Fluid region:

$$\rho\left(u\frac{\partial u}{\partial x}+v\frac{\partial u}{\partial y}\right)=-\frac{\partial p}{\partial x}+\mu\left(\frac{\partial^2 u}{\partial x^2}+\frac{\partial^2 u}{\partial y^2}\right) \qquad (3)$$

$$\rho\left(u\frac{\partial v}{\partial x}+v\frac{\partial v}{\partial y}\right)=-\frac{\partial p}{\partial y}+\mu\left(\frac{\partial^2 v}{\partial x^2}+\frac{\partial^2 v}{\partial y^2}\right) \qquad (4)$$

Momentum equation in the Porous region:

$$\frac{\rho}{\varepsilon^2}\left(u\frac{\partial u}{\partial x}+v\frac{\partial u}{\partial y}\right)=-\frac{\partial p}{\partial x}+\frac{\mu}{\varepsilon}\left(\frac{\partial^2 u}{\partial x^2}+\frac{\partial^2 u}{\partial y^2}\right)-\frac{\mu}{K}u-\frac{\rho F\varepsilon}{\sqrt{K}}|\vec{u}|u \qquad (5)$$

$$\frac{\rho}{\varepsilon^2}\left(u\frac{\partial v}{\partial x}+v\frac{\partial v}{\partial y}\right)=-\frac{\partial p}{\partial y}+\frac{\mu}{\varepsilon}\left(\frac{\partial^2 v}{\partial x^2}+\frac{\partial^2 v}{\partial y^2}\right)-\frac{\mu}{K}v-\frac{\rho F\varepsilon}{\sqrt{K}}|\vec{u}|v \qquad (6)$$

where $|\vec{u}|=\sqrt{u^2+v^2}$

The properties of porous matrix of metal foam, *K* and *F*, for momentum equation are taken from Calmidi, (1998). These empirical correlations are shown as follows:

$$F=0.00212(1-\varepsilon)^{-0.132}\left(\frac{d_f}{d_p}\right)^{-1.63} \qquad (7)$$

$$\frac{K}{d_p^2} = 0.00073(1-\varepsilon)^{-0.224}\left(\frac{d_f}{d_p}\right)^{-1.11} \quad (8)$$

where d_f / d_p is also given as a function of the porosity:

$$\frac{d_f}{d_p} = 1.18\sqrt{\frac{(1-\varepsilon)}{3\pi}}\frac{1}{G} \quad (9)$$

where G is the shape function:

$$G = 1 - e^{-(1-\varepsilon)/0.04} \quad (10)$$

It should be noted that different values of ε were chosen in this study which correspond to d_f and d_p values as shown in Table 1. F and K values which were calculated from equations (7) and (8) respectively which also are presented in Table 1. Corresponding fluid flow boundary conditions:

inlet at $x = 0$: $u = u_o 6(y/H)\left[1 - (y/H)\right]$ $v = 0$ (fully developed flow) (11a)

lower plate at $y = 0$: $u = 0$ $v = 0$ (no-slip condition) (11b)

upper plate at $y = H$: $u = 0$ $v = 0$ (no-slip condition) (11c)

exit at $x = L$: $\frac{\partial u}{\partial x} = 0$, $v = 0$ (fully developed flow) (11d)

Matching conditions are applied at the fluid-porous interface, (i.e. the continuity of velocity components and stresses are invoked). The governing energy equations are written for the metal-foam and fluid phase based on the local thermal equilibrium between them:

Energy equation in the fluid region:

$$u\frac{\partial T}{\partial x} + v\frac{\partial T}{\partial y} = \frac{k}{\rho c_p}\left(\frac{\partial^2 T}{\partial x^2} + \frac{\partial^2 T}{\partial y^2}\right) \quad (12)$$

Energy equation porous region:

$$u\frac{\partial T}{\partial x} + v\frac{\partial T}{\partial y} = \frac{k_{eff}}{\rho c_p}\left(\frac{\partial^2 T}{\partial x^2} + \frac{\partial^2 T}{\partial y^2}\right) \quad (13)$$

where $k_{eff} = \varepsilon k_f + (1-\varepsilon)k_s$. Corresponding energy boundary conditions:

inlet $(x = 0)$: $T = T_o$ (14a)

lower plate ($y = 0$): $\left.\frac{\partial T}{\partial y}\right|_{y=0} = 0$

(14b)

upper plate ($y = H$): $\left.\frac{\partial T}{\partial y}\right|_{y=H} = \begin{cases} 0 & \text{insulated walls} \\ -\frac{q''}{k_{eff}} & \text{horizontal walls adjecent to blocks} \\ -\frac{q''}{k} & \text{horizontal walls adjecent to fluid} \end{cases}$

(14c)

exit ($x = L$): $\frac{\partial T}{\partial x} = 0$

(14d)

Continuity of temperatures and heat flux are also invoked at fluid-porous interface regions.

Nondimensional Form

The governing equations and closure conditions are normalized, utilizing the following parameters:

$$X = \frac{x}{H},\ Y = \frac{y}{H}$$

$$U = \frac{u}{u_\infty},\ V = \frac{v}{u_\infty},\ P = \frac{p}{\rho u_\infty^2},\ \theta = \frac{T - T_\infty}{q\left(H / k_{eff}\right)}$$

$$R_c = \frac{k_{eff}}{k},\ \mathrm{Da} = \frac{K}{H^2},\ C = F \cdot \varepsilon,\ \mathrm{Re} = \frac{\rho u_\infty H}{\mu},\ \mathrm{Pr} = \frac{\mu c_p}{k}$$

Again, for simplification, the angle brackets representing volume-averaged variables are dropped in equation pertaining to the porous domain. Therefore, the normalized governing equations are as follows, continuity:

$$\frac{\partial U}{\partial X} + \frac{\partial V}{\partial Y} = 0 \qquad (15)$$

Equations (2–5) may be combined in a single form for both fluid and porous domains and then written in a dimensionless form as:

Momentum:

$$\frac{1}{\varepsilon^2}\left(U\frac{\partial U}{\partial X} + V\frac{\partial U}{\partial Y}\right) = -\frac{\partial P}{\partial X} + \frac{1}{\varepsilon \cdot \mathrm{Re}}\left(\frac{\partial^2 U}{\partial X^2} + \frac{\partial^2 U}{\partial Y^2}\right) - \frac{1}{\mathrm{Da}\,\mathrm{Re}}U - \frac{C}{\sqrt{\mathrm{Da}}}\left|\vec{U}\right|U \qquad (16)$$

$$\frac{1}{\varepsilon^2}\left(U\frac{\partial V}{\partial X} + V\frac{\partial V}{\partial Y}\right) = -\frac{\partial P}{\partial Y} + \frac{1}{\varepsilon \cdot \mathrm{Re}}\left(\frac{\partial^2 V}{\partial X^2} + \frac{\partial^2 V}{\partial Y^2}\right) - \frac{1}{\mathrm{Da}\,\mathrm{Re}}V - \frac{C}{\sqrt{\mathrm{Da}}}\left|\vec{U}\right|V \qquad (17)$$

In fluid region, the porosity ε and the Darcy number Da are respectively set equal to unity and infinity. Boundary conditions are:

inlet at $X = 0$: $U = 6(Y)[1- Y]$ $V = 0$ (18a)

lower plate at $Y = 0$: $U = 0$ $V = 0$ (18b)

upper plate at $Y = 1/2$: $U = 0$ $V = 0$ (18c)

exit at $X = L / D_h$: $\dfrac{\partial U}{\partial X} = 0$ $V = 0$ (18d)

Similar to the flow field, the governing Eqs. (11) and (12) for the thermal field are combined into a single equation as follows:

$$U\frac{\partial \theta}{\partial X} + V\frac{\partial \theta}{\partial Y} = \frac{R_c}{\mathrm{Re}\ \mathrm{Pr}}\left(\frac{\partial^2 \theta}{\partial X^2} + \frac{\partial^2 \theta}{\partial Y^2}\right) \tag{19}$$

where R_c is set to unity in the fluid region. Non-dimensional boundary conditions are:

inlet at $X = 0$: $\theta = 0$ (20a)

lower plate at $Y = 0$: $\left.\dfrac{\partial \theta}{\partial Y}\right|_{Y=0} = 0$ (20b)

upper plate at $Y = 1/2$: $\left.\dfrac{\partial \theta}{\partial Y}\right|_{y=1/2} = \begin{cases} 0 & \text{insulation walls} \\ -\dfrac{1}{R_c} & \text{horizontal walls adjesent to blocks} \\ -1 & \text{horizontal walls adjesent to fluid} \end{cases}$ (20c)

exit at $X = L / D_h$: $\dfrac{\partial \theta}{\partial X} = 0$ (20d)

NUMERICAL METHOD

The governing equations and the boundary conditions are numerically solved using the commercial software COMSOL Multiphysics 5.2a which utilizes finite element method (FEM). The temperature, fluid velocity and the heat flux at the solid-fluid interface were coupled using multiphysics module. Triangular elements with minimum size of $4x10^{-4}$ are considered for meshing. Furthermore, highly packed mesh near the metal foam blocks and walls are utilized to capture the interface condition, wall temperature and heat flux.

RESULTS AND DISCUSSION

Results from our computational model were first compared with the numerical data from Chikh et al. (1998) for validation purposes. They studied an electronic cooling system using three regular, not metallic, porous blocks mounted on the lower plate of channel which is also heated through the lower plate (Figure 2). Comparison of streamlines with their work for Re = 500, A = 4, R_y=0.25, R_x=0.5, H = 0.5, ε = 0.6, Pr = 0.7 and two Darcy numbers are presented in Figure 2. As the permeability of the porous medium increases (i.e.Da =10^{-3}) more fluid penetrates into the blocks. Additionally, the flow rate that goes into the first block is bigger compared to the flow rate passing through the other ones leading to enhancement of heat transfer as shown in figure 2(a). However, for low Darcy number (Da ≤ 10^{-5}), the higher pressure of the flow in the area closer to the center of the channel compared to the area between the blocks results in recirculation of the fluid in these zones as shown in figure 2 (b). The resulting vortices prevents the fluid from flowing through the next porous block and as a result from the second block onwards, the metal foams tend to act relatively as solid non-permeable slabs.

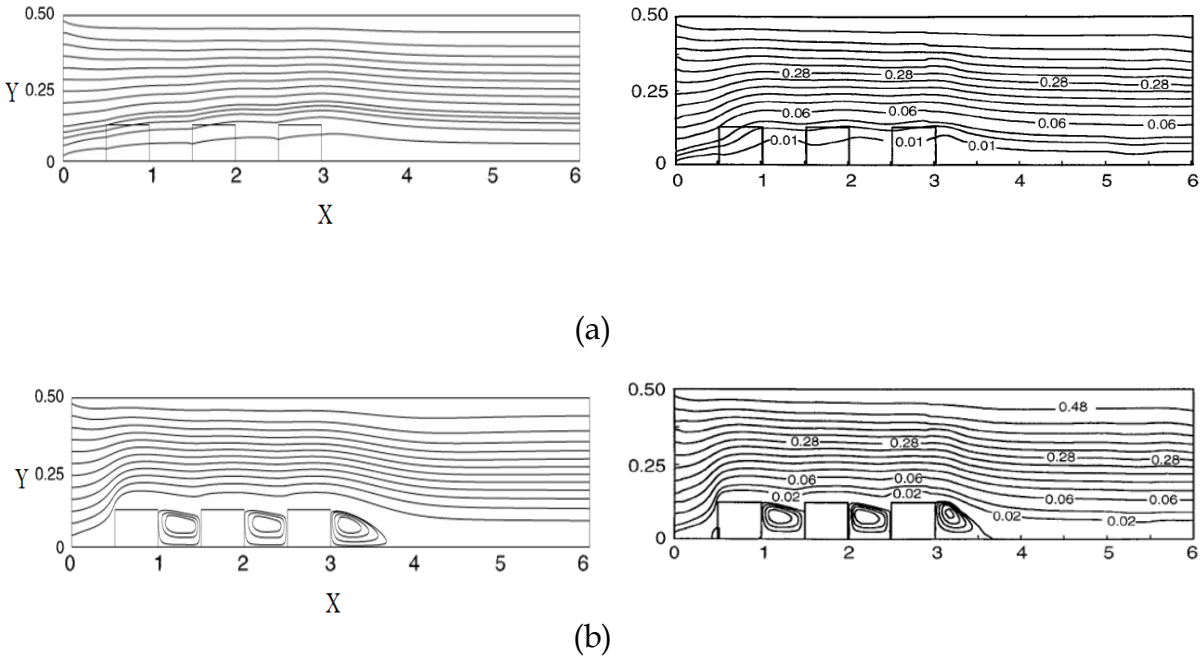

Figure 2. Streamlines Validation with Chikh et al. (1998) Results for The Same Stream Function Values at Re = 500, R_x = 0.5 and A= 4: (a) Da = 10^{-3}, (b) Da=10^{-5}.

Figure 3 (a) shows the comparison of the dimensionless wall temperature profile for Re = 500 and A = 4 with Chikh et al. (1998) for thermal conductivity ratios as high as R_c = 100. It is clearly shown that the presence of the porous blocks will reduce the wall temperature as the Da increases compared to the pure fluid case. For example, when Da = 10^{-3} and Da = 10^{-5} the average decrement in the wall

temperature was found to be 56% and 18% respectively compared to the case without any blocks.

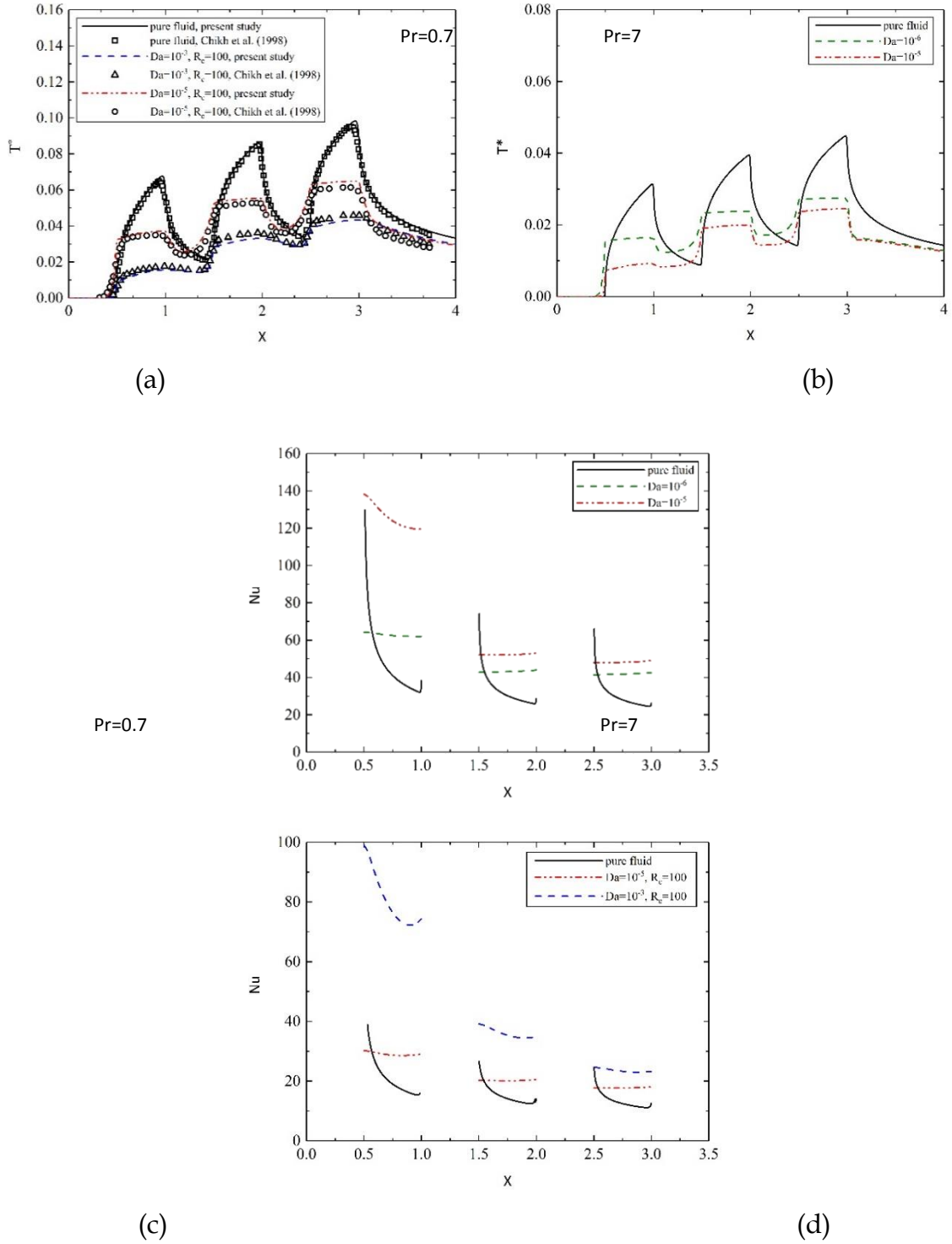

Figure 3. (a) Comparison of Dimensionless Wall Temperature with Those of Chikh et al. (1998) Results, (b) Dimensionless Wall Temperature Profile for Water Flow, (c and d) Local Nusselt Number Along The Axial Direction for Re=500 and A=4.

We increased Prandlt number from 0.7 (air) to 7 (water) (Figure 3 (b)); which leads to increase in the thermal entrance length and substantially decreases the wall temperature; which ultimately increases the Nusselt number, particularly in the first block as shown in figures 3 (c and d). When air is used, the average rate of heat transfer enhancement through the first block (compared to the case without porous blocks) is found to be 278% and 135%, for Da = 10^{-3} and Da = 10^{-5} respectively. Since using multiple blocks results in a considerable pressure drop penalty, it restricts their implementation for practical purposes. In other words, applying one porous block seems to be desirable for further energy efficiency in certain thermal applications with limitations on the pumping power, such as electronic cooling. Nevertheless our results are in very good agreement with Chikh et al. (1998) numerical results, which establishes our computational model as robust and reliable to study the setting at hand.

The aluminum foam heat sinks are employed in the present study as shown in figure 1. The solid materials are made of aluminum-alloy and its corresponding properties are shown in table 1. Water is used as the working fluid (ρ=998.2 kg/m^3 and k=0.6 W/m K). The effect of some important parameters such as porosity ($0.85 \leq \varepsilon \leq 0.95$), Darcy number ($1.72\text{x}10^{-5} \leq Da \leq 4.58\text{x}10^{-5}$) and Reynolds number ($250 \leq Re \leq 1000$) on the hydrodynamic and thermal behavior of the model is explored. Furthermore, the fluid enters the channel with uniform temperature and parabolic velocity profile representing fully developed conditions. To illustrate the effect of the aforementioned physical parameters, results (Nu and the flow) are only presented in the area with the blocks and the heat source as well as their vicinity.

Table 1. Properties of Metal-Foams for Various Porosities. Calmidi et al. (2000)

metal-foam	ε	d_f (mm)	d_p (mm)	Da	F	ρ (kg/m^3)	k (W/m K)
aluminum-alloy T6201	0.85	0.4	2.62	1.72E-05	0.058	2690	218
	0.90	0.4	3.02	2.92E-05	0.078		
	0.95	0.4	3.32	4.58E-05	0.099		

Figure 4 shows the local Nusselt number along the heated wall for aluminum-alloy T6201. As Darcy number increases the heat exchange rate between the solid and the fluid phases inside the porous metal-foam region becomes more considerable. It can be seen from figure 4 that the Darcy number has a significant impact on the local Nusselt number distribution, especially inside the first metal-foam block. As porosity increases to 0.95 and subsequently Da increases to $4.58\text{x}10^{-5}$, the average rate of increment in the Nusselt number was found to be 13%. Therefore, it can be concluded that Darcy number plays a prominent role in heat transfer enhancement of the porous metal foam compared to lower porosity cases.

Figure 4 (b) shows the local Nusselt number for ε=0.95 and Da=$4.58\text{x}10^{-5}$ at different Reynolds numbers. It is clear that the Nusselt number is directly

proportional to the Re. The maximum enhancement ($Nu_{Re=1000}/Nu_{Re=250}$) in this study was found to be 301% at ε =0.95.

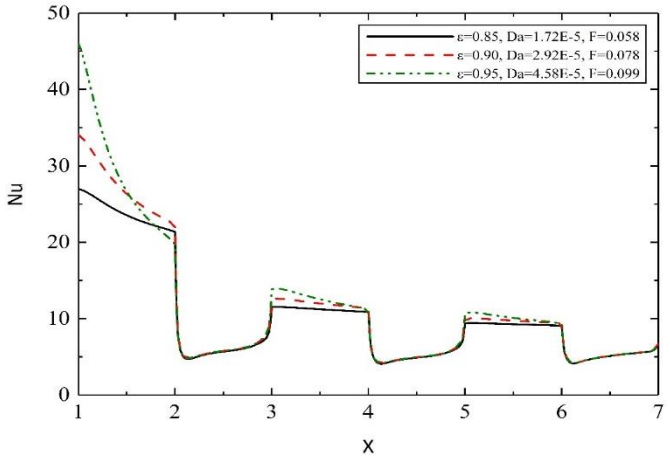

(a)

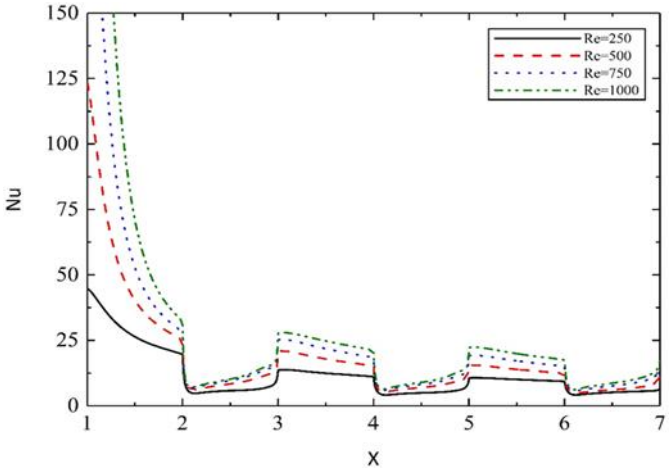

(b)

Figure 4. Local Nusselt Number Along The Channel Axis for Aluminum-Alloy T6201 at: (a) Re=250 and Different Porosities, (b) ε =0.95, Da=4.58x10^{-5}, F=0.099 and Different Reynolds Number.

Figure 5 shows the streamlines and dimensionless temperature contours for different Reynolds numbers. At high Reynolds numbers (i.e. Re=1000), the size of recirculation zones between the blocks increases and their center is pushed towards channel central region. From the isotherm contours, highest values of isothermal lines are localized near the heated wall and gradually fading towards the core region, due to the fact that the conduction heat transfer is more dominant in this part. As such, the temperature gradient and isothermal density near the wall increases when Reynolds number increases.

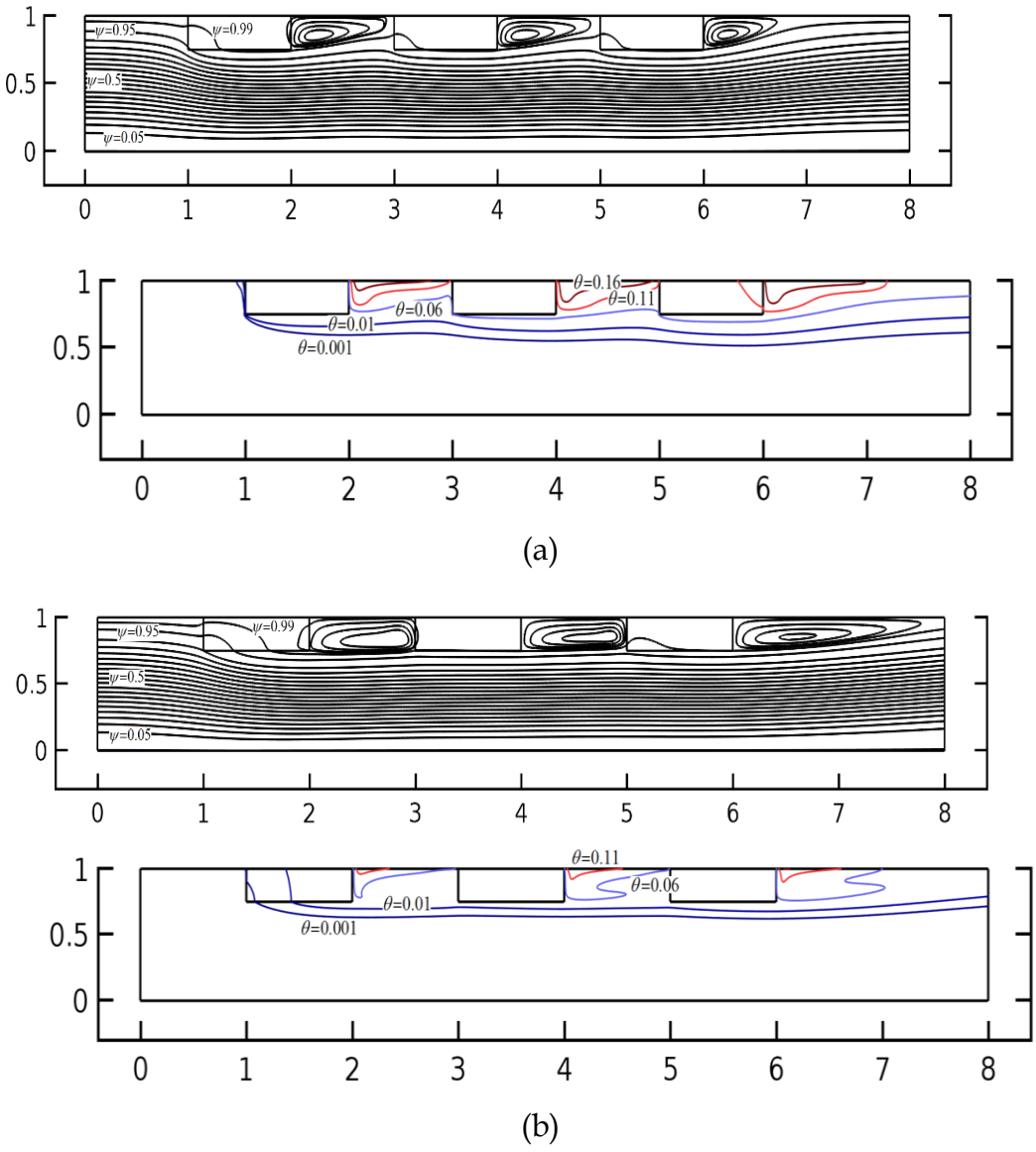

Figure 5. Streamlines and Dimensionless Temperature Contours Respectively for ε =0.95, Da=4.58x10^{-5} and F=0.099 at: (a) Re=250, (b) Re=1000.

CONCLUSION

Heat transfer in a parallel-plate solar water channel with integrated aluminum-alloy metal foam blocks has been studied numerically. For the porous region, the Brinkman-Forchheimer extension of the Darcy law was applied while Local thermal equilibrium was assumed between water, as the working fluid and the metallic porous section. Our results show that Darcy number plays a significant role in heat transfer enhancement compared to parameters such as porosity or the inertial coefficient of the blocks. Moreover, it is observed that most of the enhancement is resulted from the interactions between the fluid and the first porous block. Therefore, one block would be a better choice in certain applications

with pumping power limitations. The maximum thermal enhancement for the studied configurations shows 3 times increase in Nusselt number compared to the case with no blocks. Based on the results, metal foam heat exchangers can be considered as a promising solution to increase heat transfer enhancement in applications such as solar collectors and electronic cooling applications.

RECOMMENDATIONS

Nanofluids flow such as Al_2O_3 can be considered as an extra type of heat transfer enhancement coupled with metal-foam blocks.

REFERENCES

Albojamal, A., Vafai, K. (2017) 'Analysis of single phase, discrete and mixture models, in predicting nanofluid transport', International Journal of Heat and Mass Transfer, Vol. 114, pp. 225–237. http://www.sciencedirect.com/science/article/pii/S001793101732077X

Angirasa, D.(2002) 'Forced Convective Heat Transfer in Metallic Fibrous Materials', Journal of Heat Transfer, Vol. 124, pp. 739–745. http://heattransfer.asmedigitalcollection.asme.org/article.aspx?articleid=1445893

Banhart, J. (2001) 'Manufacture, characterisation and application of cellular metals and metal foams', Progress in Materials Science, Vol. 46, pp. 559–632. http://www.sciencedirect.com/science/article/pii/S0079642500000025

Bashria, A., Yousef, A., Adam, N.M., Sopian, K., Zaharim , A., Alghoul, M. (2007) 'Analysis of Single and Double Passes V-Grooves Solar Collector With and Without Porous Media', International Journal of energy and environment, Vol. 1, pp. 109–114. https://www.researchgate.net/publication/241906626

Calmidi, V. V. (1998). Transport phenomena in high porosity metal foams. Ph.D. Thesis, University of Colorado, Boulder, CO. Retrieved from http://abcm.org.br/anais/encit/2000/arquivos/palestras/mahajan.pdf

Calmidi, V. V., & Mahajan, R. L. (2000). Forced convection in high porosity metal foams. Retrieved from http://heattransfer.asmedigitalcollection.asme.org/article.aspx?articleid=1444400

Chabane, F., Hatraf, N., Moummi, N. (2014) 'Experimental study of heat transfer coefficient with rectangular baffle fin of solar air heater', Front. Energy, Vol. 8, pp. 160–172. https://link.springer.com/article/10.1007/s11708-014-0321-y

Chikh, S., Boumedien, A., Bouhadef, K., Lauriat , G. (1998) 'Analysis of fluid flow and heat transfer in a channel with intermittent heated porous blocks', Heat and Mass Transfer, Vol. 33, pp. 405–413. https://link.springer.com/article/10.1007/s002310050208

Kalogirou, S.A. (2004) 'Solar thermal collectors and applications', Progress in Energy and Combustion Science, Vol. 30, pp. 231–295. http://www.sciencedirect.com/science/article/pii/S0360128504000103

Kudish, A.I., Evseev, E.G., Walter, G., Leukefeld, T. (2014) 'Simulation study of a solar collector with a selectively coated polymeric double walled absorber plate', Energy Conversion and Management, Vol. 43, pp. 651–671. http://www.sciencedirect.com/science/article/pii/S0196890401000668

Lee, D.Y., Vafai, K. (1999) 'Analytical characterization and conceptual assessment of solid and fuid temperature differentials in porous media', International Journal of Heat and Mass Transfer, Vol. 42, pp. 312-324. http://www.sciencedirect.com/science/article/pii/S0017931098001859

Lu, T.J., Stone, A.H., Ashby, M.F. (1998) 'Heat transfer in open-cell metal foams', Acta mater, Vol. 46, pp. 3619–3635. http://www.sciencedirect.com/science/article/pii/S1359645498000317

Lu, W., Zhang, T., Yang, M., Wu, Y. (2017) 'Analytical solutions of force convective heat transfer in plate heat exchangers partially filled with metal foams', International Journal of Heat and Mass Transfer, Vol. 110, pp. 476–481. http://www.sciencedirect.com/science/article/pii/S0017931016326060

Lu, W., Zhao, C.Y., Tassou, S.A. (2006) 'Thermal analysis on metal-foam filled heat exchangers. Part I: Metal-foam filled pipes', International Journal of Heat and Mass Transfer, Vol. 49, pp. 2751–2761. http://www.sciencedirect.com/science/article/pii/S0017931006000524

Patankar, S.V. (1980) 'Numerical heat transfer and fluid flow', Mc Graw Hill, New York.

Qu, Z.G., Xu, H.J., Tao, W.Q. (2012) 'Fully developed forced convective heat transfer in an annulus partially filled with metallic foams: An analytical solution', International Journal of Heat and Mass Transfer, Vol. 55, pp. 7508–7519. http://www.sciencedirect.com/science/article/pii/S0017931012005844

Reddy, K.S., Satyanarayana, G.V. (2008) 'Numerical study of porous finned receiver for solar parabolic through concentrator', Engineering Applications of Computational Fluid Mechanics, Vol. 2, pp. 172–184. https://www.researchgate.net/publication/308086401

Wang, V.C., Chen, C.K. (2002) 'Forced convection in a wavy-wall channel', International Journal of Heat and Mass Transfer, Vol. 45, pp. 2587–2595. http://www.sciencedirect.com/science/article/pii/S0017931001003350

Xu, H., Gong, L., Huang, S., Xu, M. (2015) 'Flow and heat transfer characteristics of nanofluid flowing through metal foams, International Journal of Heat and Mass Transfer, Vol. 83, pp. 399–407. http://www.sciencedirect.com/science/article/pii/S0017931014011144

Zhao, C.Y. (2014) 'Review on thermal transport in high porosity cellular metal foams with open cells' International Journal of Heat and Mass Transfer, Vol. 55, pp. 3618–3632. http://www.sciencedirect.com/science/article/pii/S0017931012001664.